



Hydro-mechanical earthquake cycles in a poro-visco-elasto-plastic fluid-bearing fault structure

Luca Dal Zilio^{a,*}, Betti Hegyi^b, Whitney Behr^b, Taras Gerya^c

^a Seismology and Geodynamics, Institute of Geophysics, Department of Earth Sciences, Swiss Federal Institute of Technology (ETH Zürich), Zürich, Switzerland

^b Structural Geology and Tectonics, Geological Institute, Department of Earth Sciences, Swiss Federal Institute of Technology (ETH Zürich), Zürich, Switzerland

^c Geophysical Fluid Dynamics, Institute of Geophysics, Department of Earth Sciences, Swiss Federal Institute of Technology (ETH Zürich), Zürich, Switzerland

ARTICLE INFO

Keywords:

Rock-Fluid Interaction
Earthquake Cycles
Fault Mechanics
Poro-Visco-Elasto-Plastic Rheology
Finite Difference

ABSTRACT

A major goal in earthquake physics is to derive a constitutive framework for fault slip that captures the dependence of shear strength on fault rheology, sliding velocity, and pore-fluid pressure. In this study, we present H-MEC (Hydro-Mechanical Earthquake Cycles), a newly-developed two-phase flow numerical framework — which couples solid rock deformation and pervasive fluid flow — to simulate how crustal stress and fluid pressure evolve during the earthquake cycle. This unified, continuum-based model, incorporates a staggered finite difference–marker-in-cell method and accounts for inertial wave-mediated dynamics and fluid flow in poro-visco-elasto-plastic compressible medium. Global Picard-iterations and an adaptive time stepping allow the correct resolution of both long- and short-time scales, ranging from years to milliseconds. We present a comprehensive in-plane strike-slip setup in which we test analytical poroelastic benchmarks of pore-fluid pressure diffusion from an injection point along a finite fault width. We then investigate how pore-fluid pressure evolution and solid–fluid compressibility control sequences of *seismic* and *aseismic* fault slip. While the weakening phase is controlled by localized compaction of pores and dynamic self-pressurization of fluids inside the undrained fault zone, the subsequent propagation of dynamic ruptures is driven by pore-pressure waves. Furthermore, pore-fluid pressure conditions on the fault and shear strength weakening associated with rapid self-pressurization of fluids control the characteristic slip-weakening distance, the final size of seismic events, and the scaling between slip and fracture energy observed for large earthquakes. Our modeling results demonstrate that fault failure can occur due to poroelastic coupling on a finite-width shear zone, thus highlighting the importance of considering the realistic hydro-mechanical structure of faults to investigate fluid-driven *seismic* and *aseismic* slip, either as a natural process or induced by human activities.

1. Introduction

There is a growing interest in understanding how geologic faults respond to transient sources of fluid. This issue has become a societal concern due to the increasing interest in geothermal energy (e.g., Grigoli et al., 2017; Terakawa et al., 2012), CO₂ storage (Zoback and Gorelick, 2012), or injection of waste waters associated with hydraulic fracking (Ellsworth, 2013). Natural and artificial sources of fluid can elevate pore-fluid, which can destabilize active faults through either slow-slip or fast, seismic-wave-producing rupture events perceived as earthquakes. Examples of fluid-driven seismic and aseismic slip on natural faults are related to seismic swarms (e.g., Roland and McGuire, 2009; Chen et al., 2012; Hainzl, 2004; Hatch et al., 2020; Ross et al., 2020), aftershock

sequences (e.g., Nur and Booker, 1972; Ross et al., 2017; Miller et al., 2004; Miller, 2020), and other natural phenomena such as slow-slip events and tectonic tremors (e.g., Bürgmann, 2018; Jolivet and Frank, 2020; Behr and Bürgmann, 2021). On the other hand, fluid injections associated with human activities are well known to lead to the reactivation of faults, slow-slip transients, and earthquakes, which occasionally are large enough to cause damage (e.g., Guglielmi et al., 2015; Deichmann and Giardini, 2009; Ellsworth et al., 2019; Keranen et al., 2013, 2014; Raleigh et al., 1976; Bao and Eaton, 2016). Taken together, this body of work suggest that fluid-driven seismic and aseismic fault slip in nature and anthropogenic fluid injections are closely linked.

The propagation of fluid-driven shear cracks, the evolution of pore pressure, and the poroelastic response of faults, have been subjects of

* Corresponding author.

E-mail address: luca.dalzilio@erdw.ethz.ch (L. Dal Zilio).

interest for decades in the earthquake modeling community (e.g., Rice and Cleary, 1976; Rice, 1992; Dunham and Rice, 2008; Rudnicki and Rice, 2006; Cruz-Atienza et al., 2018; Heimisson et al., 2019; Zhu et al., 2020; Petrini et al., 2020). Recent modeling efforts have mostly focused on the stability of frictional slip when a fluid is locally injected and diffuses within a fault (Bhattacharya and Viesca, 2019; Cappa et al., 2018; Garagash and Germanovich, 2012; Larochelle et al., 2021; Yang and Dunham, 2021), or when fluid injection initiates shear cracks on a strengthening rate-and-state frictional fault (Dublanchet, 2019). Despite the apparent relevance of fluid-driven slow and fast slip transients in a wide variety of natural and anthropogenic environments, the spatio-temporal evolution of sequences of *seismic* and *aseismic* slip in response to pore-fluid evolution remains poorly constrained. This is, in part, due to the challenge of solving a fully coupled solid-fluid system in which the dynamic evolution of fault slip, stress, pore-fluid pressure, and shear strength are unknown.

In this study, we present H-MEC (Hydro-Mechanical Earthquake Cycles), a continuum-based modeling approach to solve fully dynamic sequences of seismic and aseismic slip (SEAS) in a poro-visco-elasto-plastic compressible medium with rate-dependent strength, which considerably extends our previous numerical model developed for incompressible media with rate-independent strength (Petrini et al., 2020). The computational framework is developed for the two-dimensional plane strain problem on a simplified strike-slip fault. Our coupled system utilizes Global Picard-iterations with a fully implicit adaptive time to efficiently solve all stages of the earthquake cycle. We apply a staggered finite difference-marker-in-cell (SFD-MIC) method, as it is easy to implement, flexible, and the marker-in-cell technique is often used to resolve highly deforming materials, such as faults and geologic structures (Gerya and Yuen, 2007; Petrini et al., 2020).

The goal of this study is to provide a quantitative set of numerical experiments in which we test analytical benchmarks and illustrative examples of sequences of *seismic* and *aseismic* slip along with results from the solid-fluid coupling, fluid transport on- and off-fault, pore pressure evolution, and fault slip. Our focus is to demonstrate the validity of our methodology and highlight the mechanical response of a fault zone from the solid-fluid coupling. We apply this methodology in the context of a simple, 2-D plane strain model of a strike-slip fault in a homogeneous bulk domain, which is an idealization of a natural strike-slip fault. In Section 2, we present the conceptual and mathematical model and state the continuum problem solved in this work. In Section 3, we present results of two analytical benchmarks and a set of simulations of earthquake sequences. In Section 4 we analyze and interpret the results and compare solutions for different confining pressure, solid and fluid compressibility, porosity, and fracture energy. Lastly, we discuss possible applications of this methodology for future research.

2. Methodology

2.1. Governing equations

The physical description of a deforming continuum in a static gravity field is given by the following set of conservation equations for total momentum (solid matrix and fluid; Eq. (1)), fluid momentum (Eq. (2)), fully compressible solid mass (Eq. (3)), and fully compressible fluid mass (Eq. (4)):

$$\nabla \cdot \underline{\underline{\sigma}} + g \rho^{[t]} = \rho^{[t]} \frac{D^{[s]} v^{[s]}}{D t}, \quad (1)$$

$$v^{[D]} = -\frac{k^{[\phi]}}{\eta^{[f]}} (\nabla p^{[f]} - \rho^{[f]} (g - \frac{D^{[f]} v^{[f]}}{D t})), \quad (2)$$

$$\nabla \cdot v^{[s]} = -\frac{1}{K^{[d]}} (\frac{D^{[s]} p^{[t]}}{D t} - \alpha \frac{D^{[f]} p^{[f]}}{D t}) - \frac{p^{[t]} - p^{[f]}}{\eta^{[\phi]} (1 - \phi)}, \quad (3)$$

$$\nabla \cdot v^{[D]} = \frac{\alpha}{K^{[d]}} (\frac{D^{[s]} p^{[t]}}{D t} - \frac{1}{B} \frac{D^{[f]} p^{[f]}}{D t}) + \frac{p^{[t]} - p^{[f]}}{\eta^{[\phi]} (1 - \phi)}. \quad (4)$$

Superscripts [s], [f], [t], and [D] stand for *solid*, *fluid*, *total* (solid and fluid) matrix, and *Darcy*, respectively. $\underline{\underline{\sigma}}$ is the Cauchy stress tensor, ϕ is the porosity, $\rho^{[s]}$ is the *solid* density, $v^{[s]}$ is the *solid* velocity vector, t is the time, $v^{[D]}$ represents the *Darcy flux* vector ($v^{[D]} = \phi (v^{[f]} - v^{[s]})$), i.e., the volume flux relative to the moving solid matrix, $k^{[\phi]}$ is the porosity-dependent permeability, $\eta^{[f]}$ is the *fluid* viscosity, $p^{[t]}$ and $p^{[f]}$ are the *total* and *fluid* pressure, respectively, $K^{[d]}$ is the *drained* bulk modulus, $\eta^{[\phi]}$ is the effective visco-plastic compaction viscosity, $v^{[f]}$ is the *fluid* velocity vector, α is the Biot-Willis coefficient (Biot and Willis, 1957), B is the Skempton coefficient (Skempton, 1960; Bishop, 1973), and g is the gravity vector. The total momentum (Eq. (1)) neglects differences in the solid and fluid accelerations (Gerya and Yuen, 2007; Petrini et al., 2020). Discretization of governing equations (Eqs. (1)–(4)) is given in Appendix A.

The porosity-dependent permeability is computed as

$$k^{[\phi]} = k^* (\frac{\phi}{\phi^*})^n, \quad (5)$$

where k^* and ϕ^* are the reference permeability and reference porosity (Table 1), respectively, and n is a porosity-dependent exponent, which for natural pores is assumed to be 3 (Rice, 1992; Connolly and Podladchikov, 2000), and implies that permeability changes as a cube of increasing porosity. While different k^* are tested in this study, ϕ^* is set to be 0.01 (i.e. 1%, Peacock et al., 2011) and does not evolve with time.

The *drained* bulk modulus ($K^{[d]}$), the Biot-Willis coefficient (α), and the Skempton coefficient (B) are defined as

$$K^{[d]} = (1 - \phi) (\frac{1}{K^{[\phi]}} + \frac{1}{K^{[s]}})^{-1}, \quad (6a)$$

Table 1
Model parameters.

Parameter	Symbol	Value
x-domain	L_x	100 km
y-domain	L_y	20 km
x & y grid resolution	Δ_x	100 m
Shear modulus	μ	25 GPa
Bulk modulus	K	50 GPa
Poisson ratio	ν	0.25
Total pressure	$p^{[t]}$	40 MPa
Fluid pressure	$p^{[f]}$	10 MPa
Solid density	$\rho^{[s]}$	2700 kg m ⁻³
Fluid density	$\rho^{[f]}$	1000 kg m ⁻³
Solid compressibility	$\beta^{[s]}$	2.5 10 ⁻¹¹ 1/Pa
Fluid compressibility	$\beta^{[f]}$	4.0 10 ⁻¹⁰ 1/Pa
Solid viscosity	$\eta_0^{[s]}$	10 ²³ Pa s
Fluid viscosity	$\eta^{[f]}$	10 ⁻³ Pa s
Shear wave speed	c_s	$\sqrt{\mu/\rho^{[t]}}$
Gravity	g	9.81998 m s ⁻²
Reference friction	f	0.6
Rate-strengthening parameter:		
Seismogenic zone	γ_{vw}	0.010
Lateral segments	γ_{vs}	0.100
Cohesion	c	3.0 MPa
Fault width	h	100 m
Critical nucleation size	L_c	7.3 km
Cohesive zone size	Λ_0	2.5 m
Reference velocity	V_0	10 ⁻⁹ m s ⁻¹
Reference strain rate	ϵ_0	$V_0/(2 \Delta_x)$
Reference porosity	ϕ^*	1%
Reference permeability	k^*	10 ⁻¹⁶ m ²
Loading velocity (plate rate)	V_p	2 · 10 ⁻⁹ m s ⁻¹
Inward fluid flux	p^+	+10 ⁻¹² m s ⁻¹
Outward fluid flux	\dot{p}^-	-10 ⁻¹² m s ⁻¹

$$\alpha = 1 - \frac{\beta^{[s]}}{\beta^{[d]}}, \quad (6b)$$

$$B = \frac{\beta^{[d]} - \beta^{[s]}}{\beta^{[d]} - \beta^{[s]} + \phi(\beta^{[f]} - \beta^{[s]})}, \quad (6c)$$

$$\beta^{[d]} = \frac{1 + (\beta^{[s]} K^{[\phi]})}{K^{[\phi]} - (K^{[\phi]} \phi)}, \quad (6d)$$

where $K^{[\phi]}$ the effective bulk modulus of pores, $K^{[s]}$ is the solid bulk modulus, $\beta^{[d]}$ is the compressibility of the solid skeleton (i.e., drained compressibility of the porous medium), $\beta^{[s]}$ is the compressibility of the solid phase, and $\beta^{[f]}$ is the compressibility of the fluid phase.

The stress is decomposed into a deviatoric and volumetric component:

$$\underline{\underline{\sigma}} = \underline{\underline{\tau}} - p^{[t]} \underline{\underline{I}} \quad (7)$$

where $\underline{\underline{\tau}}$ is the deviatoric stress tensor, and $\underline{\underline{I}}$ is the identity tensor. The total pressure ($p^{[t]}$) and density ($\rho^{[t]}$) are coupled with the porosity and computed from their respective fluid and solid matrix quantities

$$p^{[t]} = p^{[f]} \phi + p^{[s]}(1 - \phi), \quad (8a)$$

$$\rho^{[t]} = \rho^{[f]} \phi + \rho^{[s]}(1 - \phi), \quad (8b)$$

where $p^{[s]}$ and $\rho^{[s]}$ are solid pressure and solid density, respectively. The effective bulk modulus of pores ($K^{[\phi]}$), as well as the effective visco-plastic compaction viscosity ($\eta^{[\phi]}$) are computed following Yarushina and Podladchikov (2015) and Petrini et al. (2020) as

$$K^{[\phi]} = \frac{2m}{1+m} \frac{\mu}{\phi}, \quad (9a)$$

$$\eta^{[\phi]} = \frac{2m}{1+m} \frac{\eta_{s(vp)}}{\phi}, \quad (9b)$$

where m is a geometrical factor, μ is the shear modulus, and $\eta_{s(vp)}$ is the effective visco-plastic shear viscosity of the solid matrix. In this study m takes a value of 1 (i.e., cylindrical pores), which reduces Eqs. (9a) and (9b) to μ^*/ϕ and $\eta_{s(vp)}/\phi$. The visco-plastic effective shear viscosity in Eq. (9b) is a key component of our rheological model. In particular, the documented self-pressurization of a plastically yielding fault is a direct consequence of the assumed decrease of pores resistance to visco-plastic compaction (i.e., the decrease in $\eta^{[\phi]}$) caused by the decrease in the visco-plastic shear resistance $\eta_{s(vp)}$ during yielding.

For in-plane (mode-II) slip, the effective shear modulus, i.e., the elastic modulus for quasi-static plane strain deformation (Rubin and Ampuero, 2007), is equal to

$$\mu^* = \frac{\mu}{1 - \nu}, \quad (10)$$

Where ν is Poisson's ratio and μ is the shear modulus.

The continuity equations of both solid (Eq. (3)) and fluid (Eq. (4)) contain poroelasticity terms consistent with Biot's theory (Biot, 1941; Gassmann, 1951; Yarushina and Podladchikov, 2015), which allow for compressibility of the solid matrix and fluid as well as viscous and elastic (de)compaction of the porous space. Being Eqs. (3) and (4) fully coupled, convergence and divergence of the vector flow occur as a result of compaction/decompaction processes, which results in a fully coupled hydro-mechanical system.

2.2. Visco-elasto-plastic rheology

Components of the deviatoric deformation (strain rate) tensor are defined upon the assumption of infinitesimal strain as follows:

(6b)

$$\dot{\epsilon}_{ij}' = \frac{1}{2} \left(\frac{\partial v_i}{\partial x_j} + \frac{\partial v_j}{\partial x_i} \right) - \frac{1}{3} \text{Tr} \dot{\epsilon}_{ij}, \quad (11)$$

where i and j are arbitrary indexes and x_i and x_j are the 2-D spatial coordinates defining the tensor components. We assume that strain rate is described as a combination of elastic, viscous, and plastic components as

$$\dot{\epsilon}_{ij}' = [\dot{\epsilon}_{ij}']_{\text{viscous}} + [\dot{\epsilon}_{ij}']_{\text{elastic}} + [\dot{\epsilon}_{ij}']_{\text{plastic}}. \quad (12)$$

The elastic component is defined as

$$[\dot{\epsilon}_{ij}']_{\text{elastic}} = \frac{1}{2\mu} \frac{\tilde{D}}{Dt}(\tau_{ij}), \quad (13)$$

where the differential operator \tilde{D}/Dt describes the co-rotational time derivative of the Cauchy stress.

Viscous deformation obeys Newton's law and is defined here via an effective shear viscosity of the bulk porous material η_m composed of solid matrix and fluid

$$\eta_m = \frac{\tau_{II}'}{2\dot{\epsilon}_{II}^{[v]}}, \quad (14)$$

where τ_{II}' is the second invariant of the deviatoric stress and $\dot{\epsilon}_{II}^{[v]}$ is the viscous component of the second invariant of the strain rate. The viscous contribution to the strain rate tensor is thus defined as

$$[\dot{\epsilon}_{ij}']_{\text{viscous}} = \frac{\tau_{ij}}{2\eta_s}, \quad (15)$$

where η_s is the shear viscosity. Plastic deformation is governed by a rate-dependent strength of a non-associated plasticity model (Yi et al., 2018)

$$\tau_{\text{yield}} = \tau_0 \left(\frac{\dot{\epsilon}_{II}^{[p]}}{\varepsilon_0} \right)^\gamma, \quad (16)$$

where $\dot{\epsilon}_{II}^{[p]}$ is the second invariant of the deviatoric plastic strain rate

$$\dot{\epsilon}_{II}^{[p]} = \varepsilon_0 \left(\frac{\tau_{II}}{\tau_0} \right)^{1/\gamma}, \quad (17)$$

ε_0 is the reference strain rate, γ is the rate-strengthening exponent (Table 1), and τ_0 represents the inclusion of the Drucker–Prager yield function defining the maximum allowable shear stress a rock can withstand (Prager and Drucker, 1952)

$$\tau_0 = c + f(p^{[t]} - p^{[f]}) \quad (18)$$

where c is the cohesion strength and f is the reference, static friction coefficient. Slip rate on the fault is then computed using the second invariant of the plastic strain rate $\dot{\epsilon}_{II(p)}$ across the fault thickness h

$$V(t, x) = 2\dot{\epsilon}_{II(p)} h. \quad (19)$$

Note that the fault is represented as a finite-width shear zone and plastic deformation is calculated as volumetric strain and is represented by a tensor. As a result, plastic yielding can spontaneously localize anywhere (Dal Zilio et al., 2022). Furthermore, the rate-dependent strength (Eq. (16)) relies on the presence of γ , which mimics the positive direct effect in the rate- and state-dependent friction formulation (e.g., Scholz, 1998), a feature that has ample laboratory confirmation (Dieterich, 1979, 1981; Ruina, 1983; Marone, 1998). On the other hand, our rate-dependent strength formulation does not require the presence of an evolutionary effect involving a decrease in friction. This is because the weakening mechanism in our fully coupled system is controlled by the evolution of pore-fluid pressure ($p^{[f]}$), which is encapsulated in τ_0 (Eq. (18)).

The non-associated plastic flow law is defined through the plastic flow potential (Q), which reflects the amount of mechanical energy per unit

volume that supports plastic deformation (Vermeer, 1998)

$$Q = \tau_{II} - \sin(\psi) (p^{[t]} - p^{[f]}) - \cos(\psi)c. \quad (20)$$

Here we assume that the dilation angle ψ is zero. Accordingly, the plastic component of the deviatoric strain rate is defined as

$$[\dot{\epsilon}_{ij}']_{\text{plastic}} = \begin{cases} 0 & \rightarrow \tau_{II} < \tau_{\text{yield}} \\ \chi \frac{\partial Q}{\partial \tau_{ij}} = \chi \frac{\tau_{ij}}{\tau_{II}} & \rightarrow \tau_{II} = \tau_{\text{yield}}, \end{cases} \quad (21)$$

with χ indicating the *plastic multiplier*, which serves to ensure that, if yielding occurs, the deviatoric stress will always satisfy the yield criteria ($\tau_{II} = \tau_{\text{yield}}$).

The deviatoric components (τ_{ij}) of the stress tensor in Eq. (1) are formulated using the visco-elasto-plastic constitutive relationships (Eq. (12)) and assuming an implicit first-order finite-difference scheme in time (e.g., Moresi et al., 2003)

$$\tau_{ij} = 2\eta_{vp}Z\dot{\epsilon}_{ij}' + \tau_{ij}^0(1-Z), \quad (22a)$$

$$Z = \frac{\mu\Delta t}{\mu\Delta t + \eta_{vp}}, \quad (22b)$$

where Z is the visco-elasticity factor (Schmalholz et al., 2001), Δt is the computational time step, and η_{vp} is the effective visco-plastic viscosity of the bulk porous material that characterizes the intensity of the plastic deformation

$$\eta_{vp} = \begin{cases} \eta_m & \rightarrow \tau_{II} < \tau_{\text{yield}} \\ \eta_m \frac{\tau_{II}}{2\eta_m \dot{\epsilon}_{II,[p]} + \tau_{II}} & \rightarrow \tau_{II} = \tau_{\text{yield}}, \end{cases} \quad (23)$$

where η_m is the effective shear viscosity of the bulk porous material (Katz et al., 2006)

$$\eta_m = \eta_s e^{(\lambda\phi)}. \quad (24)$$

$\lambda = -29 \pm 3$ defines an experimentally derived porosity-weakening coefficient (Katz et al., 2006). Eq. (24) is valid for porous matrix, i.e., when the fluid fraction is relatively low (<10%).

2.3. Global visco-elasto-plastic picard iterations

We accurately satisfy the plastic yielding condition at the Eulerian nodal points of the staggered grid by using global Picard iteration (Gerya, 2019). As a result, we discretize the rate-strengthening yielding condition (Eq. (16)) to satisfy the condition $\tau_{\text{yield}} = \tau_{II}$:

$$\begin{aligned} \tau_{\text{yield}(i,j)} = & c + f \frac{1}{4} ((p_{(i,j)}^{[t]} - p_{(i,j)}^{[f]}) + (p_{(i+1,j)}^{[t]} - p_{(i+1,j)}^{[f]}) \dots \\ & + (p_{(i,j+1)}^{[t]} - p_{(i,j+1)}^{[f]}) + (p_{(i+1,j+1)}^{[t]} - p_{(i+1,j+1)}^{[f]})) (\frac{\dot{\epsilon}_{[p]}}{\epsilon_0})^\gamma, \end{aligned} \quad (25)$$

$$\begin{aligned} \tau_{II(i,j)} = & \left(\tau_{xy(i,j)}^2 + \frac{1}{2} \left(\frac{(\tau_{xx(i,j)} + \tau_{xx(i+1,j)} + \tau_{xx(i,j+1)} + \tau_{xx(i+1,j+1)})^2}{4} \right. \right. \dots \\ & + \frac{1}{2} \left(\frac{(\tau_{yy(i,j)} + \tau_{yy(i+1,j)} + \tau_{yy(i,j+1)} + \tau_{yy(i+1,j+1)})^2}{4} \right. \dots \\ & \left. \left. + \frac{1}{2} \left(\frac{(\tau_{xx(i,j)} - \tau_{yy(i,j)} + \tau_{xx(i+1,j)} - \tau_{yy(i+1,j)} + \tau_{xx(i,j+1)} - \tau_{yy(i,j+1)} + \tau_{xx(i+1,j+1)} - \tau_{yy(i+1,j+1)})^2}{4} \right)^{1/2} \right) \right) \end{aligned} \quad (26)$$

The Picard iteration is performed by repeating solution of Eqs (1)–(4) and evaluating $[\tau_{II}]_{\text{elastic}}$ at each basic node as

$$[\tau_{II}]_{\text{elastic}} = \tau_{II} \left(\frac{\mu^* \Delta t + \eta_{vp}}{\eta_{vp}} \right), \quad (27)$$

Where η_{vp} is the current local value of the effective visco-plastic viscosity of the solid matrix, which defines the relationship between the deviatoric strain rate and the deviatoric stress. When $[\tau_{II}]_{\text{elastic}} > \tau_{\text{yield}}$, we compute the new visco-plastic viscosity at the node as

$$\eta_{vp} = \mu^* \Delta t \frac{\tau_{\text{yield}}}{[\tau_{II}]_{\text{elastic}} - \tau_{\text{yield}}}. \quad (28)$$

If $\eta_{vp} < \eta_s$, the new visco-plastic viscosity from Eq. (28) is used for the next iteration. The global plastic yielding condition error is then computed on the nodal points

$$\Delta\tau_{\text{yield}} = \frac{1}{N} \sqrt{\sum_{i,j} (\tau_{II(i,j)} - \tau_{\text{yield}(i,j)})^2} \quad (29)$$

where N is the cumulative number of nodal points at which either the previously computed or new value of η_{vp} satisfies the condition $\eta_{vp} < \eta_s$. The stopping criteria of the Picard iteration is reached when $\Delta\tau_{\text{yield}}$ has decreased below a desirable level of tolerance (δ_{err})

$$\Delta\tau_{\text{yield}} \leq \delta_{\text{err}} \quad (30)$$

where $\delta_{\text{err}} = 10\text{Pa}$.

An important mechanism for fluid pressurization is the feedback between visco-plastic viscosity and *compaction viscosity* (often called bulk viscosity), which characterizes solid matrix resistance to reversible (i.e., elastic, $\rho^{[d]}$) and irreversible (i.e., visco-plastic, $\eta^{[\phi]}$) pore compaction/decompaction. When plastic yielding occurs, we first compute the plastic viscosity (η_p) at the basic nodes (b) as

$$\eta_{p(b)} = \frac{1}{1/\eta_{vp(b)} - 1/\eta_{m(b)}}. \quad (31)$$

We then compute the new plastic viscosity at the center of cells (i.e., pressure nodes, p) by using the harmonic average of the plastic viscosity values from the four surrounding basic nodes (b) (Gerya, 2019)

$$\eta_{p(p)(i,j)} = \frac{4}{1/\eta_{p(b)(i,j)} + 1/\eta_{p(b)(i-1,j)} + 1/\eta_{p(b)(i,j-1)} + 1/\eta_{p(b)(i-1,j-1)}}. \quad (32)$$

Finally we compute the new compaction viscosity at the pressure nodes as

$$\eta_{p(p)(i,j)}^{[\phi]} = \frac{1}{\phi(1/\eta_{0(p)(i,j)} + 1/\eta_{p(p)(i,j)})}, \quad (33)$$

and the new visco-plastic viscosity at the pressure nodes as

$$\eta_{vp(p)(i,j)} = \frac{1}{1/\eta_{0(p)(i,j)} + 1/\eta_{m(p)(i,j)}}, \quad (34)$$

where η_0 is the reference viscosity of the solid matrix on the pressure

nodes (Table 1).

2.4. Adaptive time-stepping

To resolve all stages of the earthquake cycle, from long-term (tectonic) deformation to periodic slip events, we introduce a variable time stepping during computation. To accomplish this, we require that the time step is the minimum of the time steps needed to resolve (1) the slip acceleration on the fault (Δt_s), (2) the displacement per grid cell (Δt_d), and (3) the visco-elasto-plastic time step (Δt_{vep}) as

$$\Delta t = \min \{\Delta t_s, \Delta t_d, \Delta t_{\text{vep}}\}. \quad (35)$$

The first time step requires that the slip acceleration per time step is limited to a fraction of the grid size as

$$\Delta t_s = \frac{\Delta x \delta_d}{V_{\max}}, \quad (36)$$

where $\delta_d = 10^{-5}$ defines the maximum grid fraction. Similarly, we require that the displacement per time step is limited by the same fraction of the grid size

$$\Delta t_d = \delta_d \min \left\{ \left| \frac{\Delta x}{V_x} \right|, \left| \frac{\Delta y}{V_y} \right| \right\}. \quad (37)$$

Based on a previous study (Herrendörfer, 2018), we apply a visco-elasto-plastic time step to capture the relaxation time scale η_{vep}/μ^* by a fraction ξ

$$\Delta t_{\text{vep}} = \xi \frac{\eta_{\text{vep}}}{\mu^*}, \quad (38)$$

where $\xi = 0.2$. Notably, the visco-elasto-plastic relaxation time step combines both the visco-elastic relaxation η_{vep}/μ^* and the elasto-plastic relaxation time scale

$$\frac{\tau_{\text{II}}}{\mu^* \chi} = \frac{\tau_{\text{II}}}{2\mu^* [\dot{\epsilon}_{ij}']_{\text{plastic}}}. \quad (39)$$

As a result, Δt_{vep} provides a constraint on the final time step when viscous deformation is dominant, thus ensuring the resolution of the relaxation time. Importantly, we do not apply any minimum time step cutoff. This is in contrast to previous studies (e.g., Lapusta and Liu, 2009), in which the time step is only adapted until it reaches $\Delta t_{\min} = (1/3) \Delta x/c_s$, where c_s is the shear wave speed (see Table 1). We do not adopt a minimum time step cutoff because during the propagation of fully dynamic ruptures the actual time step can decrease below the Δt_{\min} threshold. As a result, applying a cutoff would reduce the convergence rate during Picard iterations (Section 2.3).

2.5. Model setup and boundary conditions

The 2-D model setup consists of a strike-slip fault (Fig. 1). We consider a mode-II plane strain shear motion along a planar interface embedded in a poro-visco-elasto-plastic medium (Fig. 1). We utilize a $x - y$ Cartesian coordinate system with $y = 0$ being the sliding interface. This simple setup is designed to enable comparison to both analytical benchmarks for numerical solution and classical earthquake cycle simulations and theoretical estimates of the critical length scales during nucleation and propagation of dynamic ruptures (e.g., Lapusta et al., 2000). Parameters and physical constants are given in Table 1.

The system of equations over the domain $\Omega = [0, L_x] \times [0, L_y]$ is solved by using specific boundary conditions for pressure and velocity (Fig. 1). For the model setup of this study, the conditions on the left ($x = 0$) and right ($x = L_x$) boundaries are open and allow for horizontal shear:

$$\frac{\partial v_x}{\partial x} = 0|_{x=0}, \frac{\partial v_y}{\partial x} = 0|_{x=0}, \quad (40a)$$

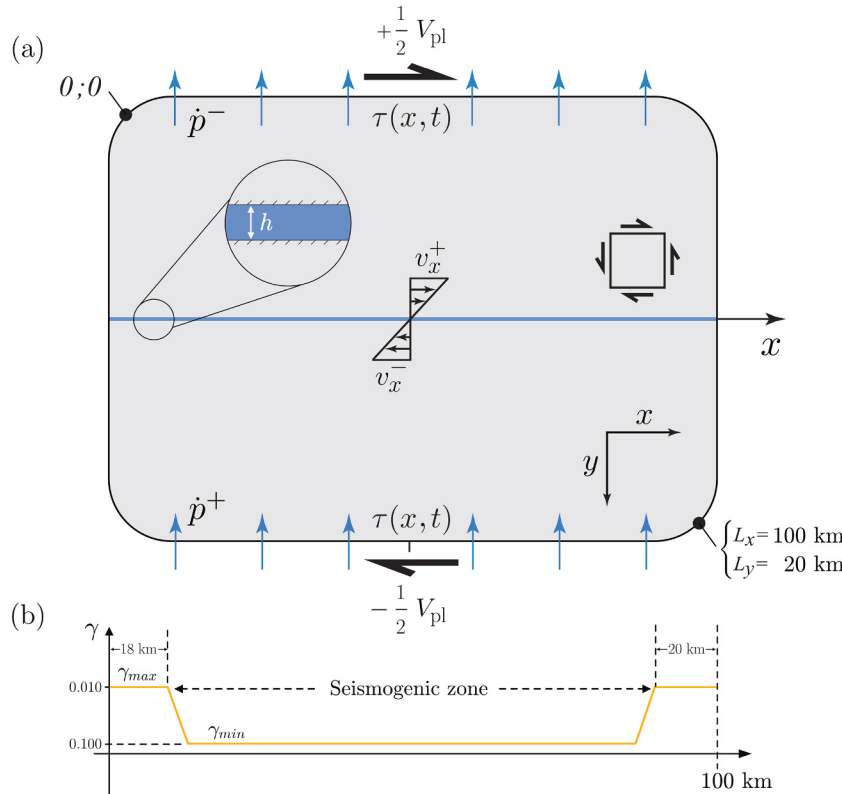


Fig. 1. Illustration of the model setup. In-plane shear zone embedded in a homogeneous poro-visco-elasto-plastic media, with the shear layer undergoing uniform strain and a relative displacement. Boundary conditions include tangential displacement (black arrows) prescribed at the top and bottom boundaries. Blue arrows at the top and bottom boundaries indicate the inflow (p^+) and outflow (p^-) boundary conditions of fluid. The seismogenic region with velocity-weakening properties is surrounded by velocity-strengthening regions. (For interpretation of the references to color in this figure legend, the reader is referred to the web version of this article.)

$$\frac{\partial v_x}{\partial x} = 0|_{x=L_x}, \frac{\partial v_y}{\partial x} = 0|_{x=L_x}. \quad (40b)$$

This condition implies that the velocity component parallel to the boundary is constant (zero shear stress), whereas the velocity component normal to the boundary does not change across the boundary. The fault is loaded from the upper ($y = 0$) and lower boundaries ($y = L_y$) by applying a constant loading rate in the form of Dirichlet boundary conditions and assuming zero velocity on the vertical component v_y (Fig. 1):

$$v_x = +\frac{1}{2}V_{pl}|_{y=0}, v_y = 0|_{y=0}; \quad (41a)$$

$$v_x = -\frac{1}{2}V_{pl}|_{y=L_y}, v_y = 0|_{y=L_y}; \quad (41b)$$

where $V_{pl} = 6.3 \text{ cm yr}^{-1}$ is the constant loading rate.

Pressure boundary conditions have to be defined for both total ($p^{[t]}$) and fluid ($p^{[f]}$) pressure. Since the solid mass (Eq. (3)) and fluid mass (Eq. (4)) are intrinsically coupled, we first initialize the fluid pressure with a constant confining pressure (p_{con}) and then we apply a constant effective pressure (p_{eff}) on the top and lower boundary:

$$p^{[t]} - p^{[f]} = p_{eff}|_{y=0, y=L_y} \quad (42)$$

Fluid momentum (Eq. (2)) is solved assuming *free slip* condition for the left and right boundaries

$$\frac{\partial v_y^{[D]}}{\partial x} = 0|_{x=0}, \quad (43a)$$

$$\frac{\partial v_y^{[D]}}{\partial x} = 0|_{x=L_x}, \quad (43b)$$

whereas an inward (\dot{p}^+) and outward (\dot{p}^-) fluid flux is defined on the top and lower boundary (Table 1) in the form of Neumann boundary conditions

$$\frac{\partial v_y^{[D]}}{\partial y} = \dot{p}^-|_{y=0}, \quad (44a)$$

$$\frac{\partial v_y^{[D]}}{\partial y} = \dot{p}^+|_{y=L_y}, \quad (44b)$$

3. Results

3.1. Fluid injection benchmarks

To test the robustness of the code in a broad range of applications relevant to solid-fluid interaction, in this section we compare our modeling results against analytical benchmarks of pore-fluid pressure diffusion. In particular, we consider two benchmark exercises (BP1 and BP2) from a set of quasi-static problems in a 2-D domain with a 1-D fault

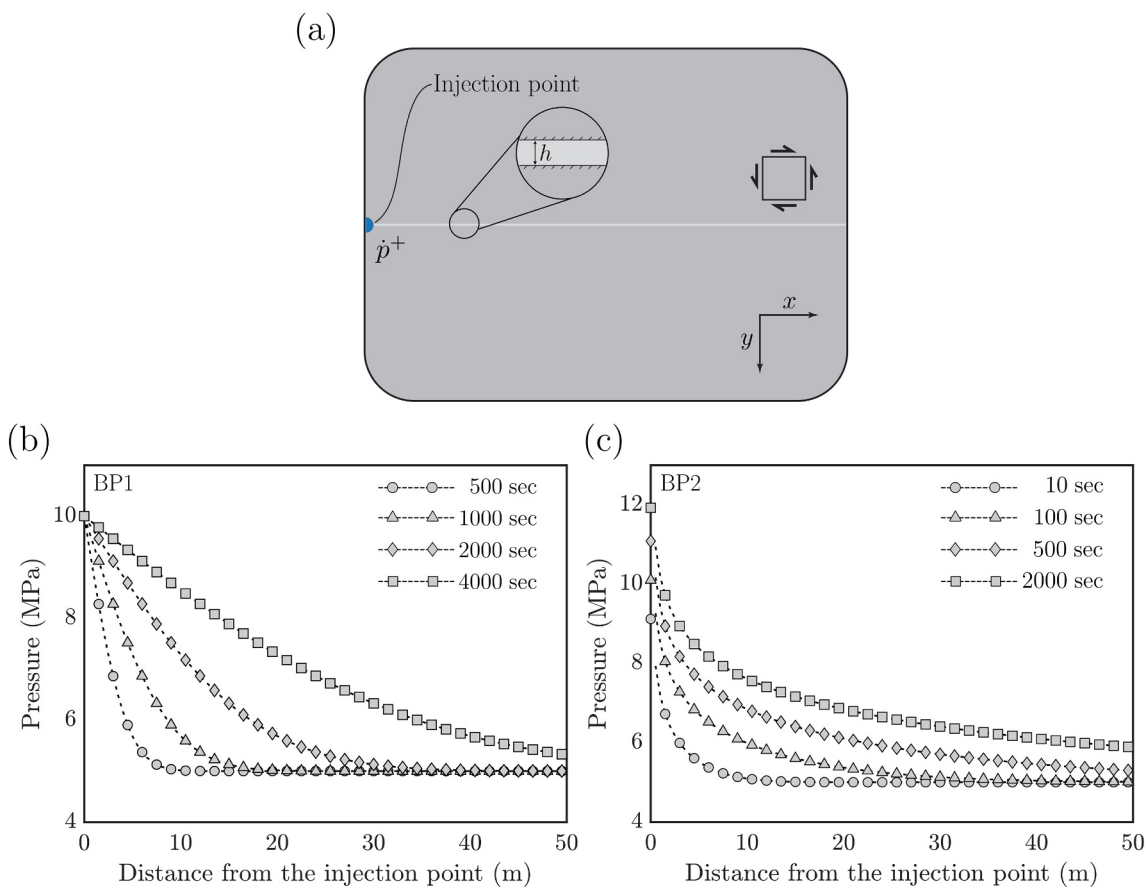


Fig. 2. Modified model setup with a source point of fluid injection and results from analytical benchmarks of pore-fluid pressure diffusion. (a) The fault is embedded within a thin poro-visco-elasto-plastic layer of finite width (h), assumed to be much more permeable than surroundings. Fluid is injected at $x = 0$ and diffuses along the fault with a diffusion timescale of $\sqrt{4\alpha t}$, with α indicating the constant hydraulic diffusivity (Eq. (46)). For this specific set of experiments, $p_0^{[f]} = 5 \text{ MPa}$, $\phi = 1\%$, $\eta^{[f]} = 10^{-3} \text{ Pa s}$, $k^{[\phi]} = 10^{-17} \text{ m}^2$ and the fault width $h = 1 \text{ m}$. (b) First benchmark problem (BP1), which simulates fluid injection as a source of constant fluid pressure $\Delta p^{[f]} = 5 \text{ MPa}$. The black dashed lines indicate the analytical solution following Eq. (45), whereas grey markers indicate the numerical results. (c) Second benchmark problem (BP2), which simulates fluid injection at a constant volume rate of $Q_w = 2.8 \text{ l/min}$. The black dashed lines indicate the analytical solution following Eq. (47), whereas grey markers indicate the numerical results.

subjected to perturbations of fluid injection and along-fault pore-fluid diffusion. In order to verify these two benchmarks, we modify the model setup given in Section 2.5 by including an injection point on the left boundary (Fig. 2a).

For the first benchmark problem (BP1), injection is modeled as a source of constant fluid pressure ($\Delta p^{[f]}$) at $x_{inj} = x_{(0)}$. The resulting pore-fluid pressure diffusion along the interface can be solved analytically as (e.g., Viesca, 2021)

$$p^{[f]}(x, t) = p_0^{[f]} + \Delta p^{[f]} \cdot \text{erfc}\left(\frac{|x|}{l_d(t)}\right), \quad (45)$$

where erfc is the complementary error function, $l_d(t) = \sqrt{4\alpha t}$ is the diffusion lengthscale, and α is the constant hydraulic diffusivity

$$\alpha = \frac{k^{[\phi]}}{\eta^{[f]}\beta^*}, \quad (46)$$

where $\eta^{[f]}$ is the viscosity of the permeating fluid and β^* is a storage coefficient reflecting the compressibility of the fluid and porous matrix. On the other hand, the second benchmark problem (BP2) assumes a constant volume rate injection from a point source ($x_{inj} = x_{(0)}$), and the flow solution is given by Carslaw and Jaeger (1959):

$$p(x, t) - p_0 = \frac{Q_w \eta^{[f]}}{4\pi k^{[\phi]} h} E_1\left(\frac{\sqrt{(x - x_{inj})^2}}{4\alpha t}\right), \quad (47)$$

where Q_w is the constant injection volume rate, h is the fault thickness, and E_1 is the exponential integral function. Note that the fault hydraulic transmissivity represents the product $k^{[\phi]} h$.

For both benchmarks BP1 and BP2, fluid is injected into the fault and it is constrained to flow only within its hydraulic aperture, a scenario

that would occur when the permeability of the host rock is negligible relative to the fault itself (i.e. no fluid leak-off). Also, the fault is assumed *marginally pressurized* — that is, $\Delta p^{[f]}$ is always below the total pressure (in order to avoid hydraulic fracturing). Fig. 2 shows the results from the BP1 (Fig. 2b) and BP2 (Fig. 2c) and demonstrates the high accuracy of the numerical solution, which overlaps with the analytical solutions at different time stages. It is worth noting that the exponential integral function in Eq. (47) is singular at the injection point $x = x_{inj}$ (Fig. 2c). This means that, for the case of injection experiments at constant volume rate, the fluid pressure at the origin is unbounded.

3.2. Earthquake cycles

The long-term response of the fault to slow loading rate is characterized by periods of quasi-static deformation followed by slip events, either slow or fast (Fig. 3a–c), in which the slip rate on the fault accelerates from $\sim \text{cm yr}^{-1}$ to $\sim \text{m s}^{-1}$ (Fig. 3d). As a result, the adaptive time step is large (fraction of a year) during the inter-seismic periods, and small (milliseconds) during the occurrence of dynamic rupture (Fig. 3e). Similarly, the effective pressure ($p^{[t]} - p^{[f]}$) drops by ~ 20 MPa as a result of the poroelastic response of the fault zone during fast shearing (Fig. 3f).

Slip history on the fault indicate that, when assuming homogeneous properties, regular cycles of complete ruptures arises from the numerical experiments (Fig. 4). While the imposed loading rate increases stress linearly with time, slip rate increases exponentially on both the left and right side of the fault, i.e., where γ is high (Fig. 1b). Consequently, the two lateral segments of the fault steadily creep at rates comparable to the imposed loading rate (Fig. 4a), the seismogenic zone remains locked during inter-seismic periods and stress concentrates at the transition between high and low γ . In the later stages of the inter-seismic periods,

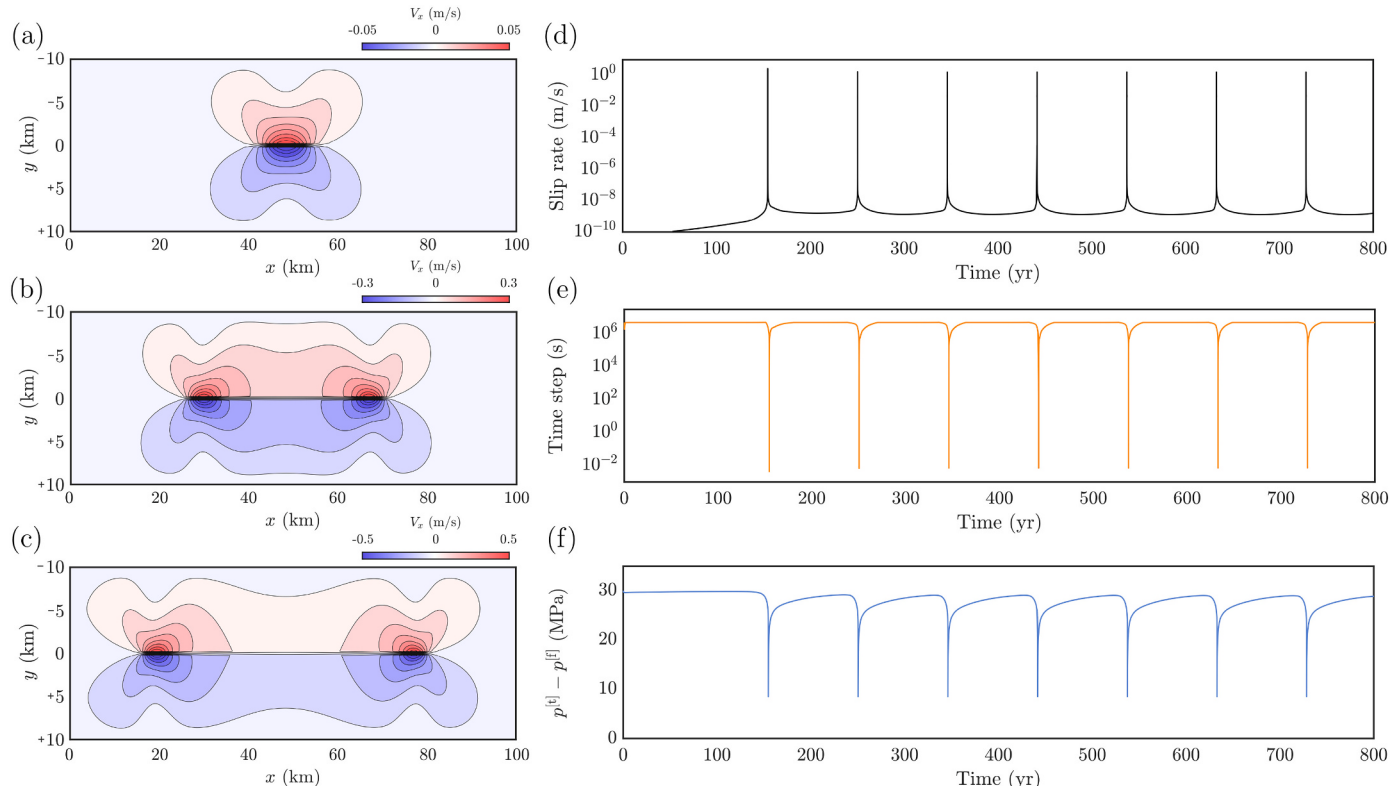


Fig. 3. Spatial horizontal velocity and temporal evolution of earthquake cycles. Evolution of the horizontal velocity (v_x) during the (a) nucleation phase and (b–c) propagation of dynamic rupture. Long inter-seismic periods are characterized by quasi-static deformation while the left and right segments of the fault zone creep at rates comparable to the loading rate. Note that the color scale of v_x velocities in (a–c) are not the same. Temporal evolution of (d) maximum slip velocity (e) time-step, and (f) effective pressure on the fault. Large time steps are used during the inter-seismic periods, whereas the propagation dynamic rupture is resolved with time steps of the order of milliseconds.

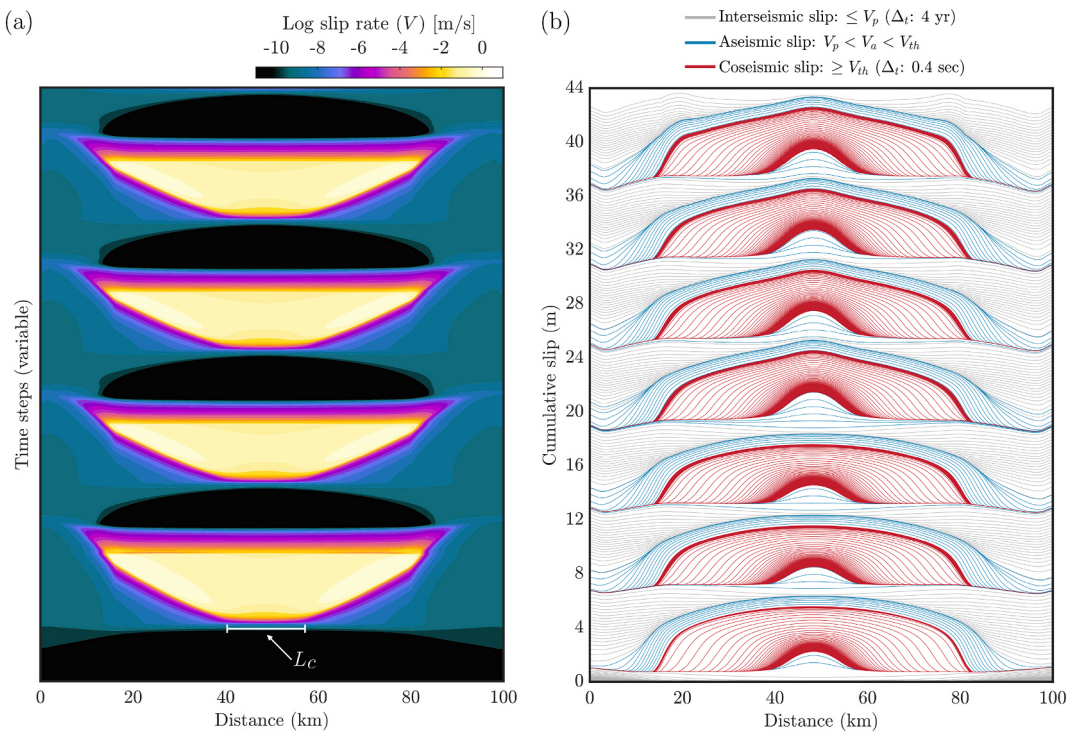


Fig. 4. (a) Slip rate history on the fault for the reference model. The y-axis displays the time step. The simulation period is 500 years, including a spin-up period of ~ 150 years. L_c indicates the critical nucleation size. Slip velocity is plotted on the logarithmic scale. (b) Cumulative slip on the fault after multiple events over a period of 800 years. Red lines indicate the co-seismic slip every 0.4 sec when the maximum slip velocity exceeds the threshold of 8.1 cm s^{-1} (see Eq. (48)), blue lines illustrate post-seismic slip transients with slip rate in between the loading rate (V_p) and the co-seismic slip velocity threshold (V_{th}). Gray lines (every 4 years) illustrate the inter-seismic (aseismic) behavior of the fault with slip rates equal or lower than the loading rate.

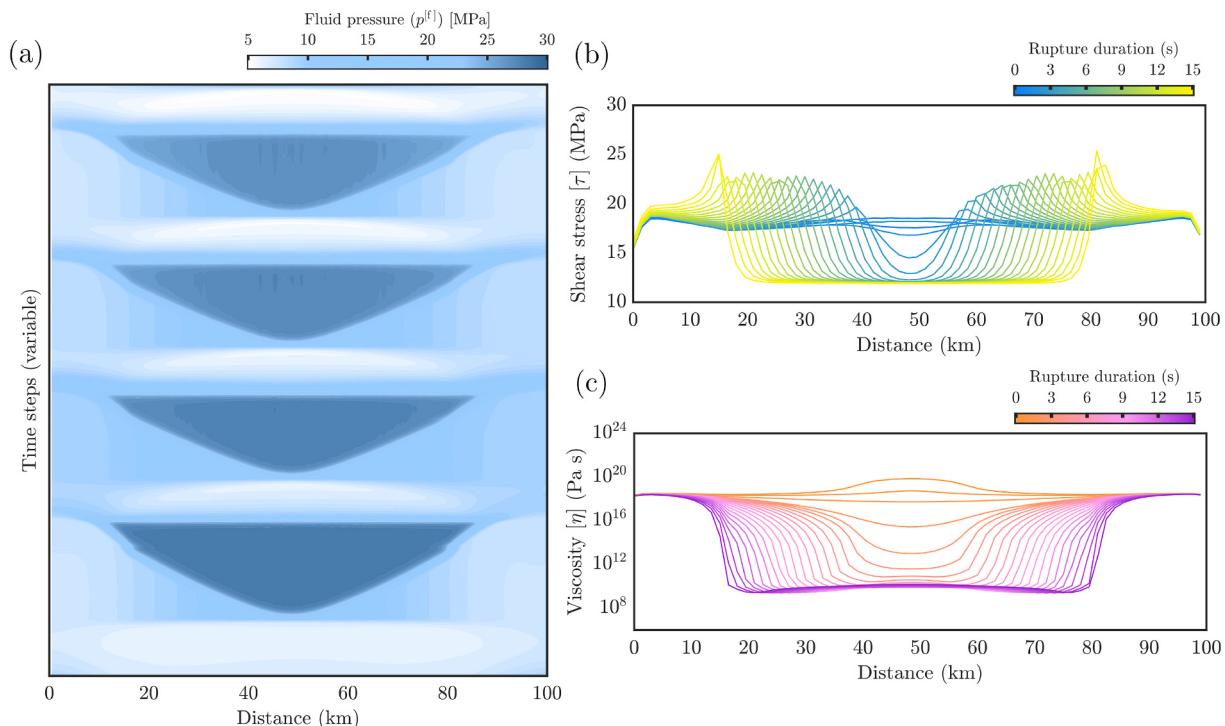


Fig. 5. (a) Long-term histories of fluid pressure on the fault for the reference model. The y-axis displays the time step, which varies by several orders of magnitude. The simulation period is 500 years, which start with a ~ 150 years spin-up period. Spatiotemporal evolution of (b) shear stress and (c) viscosity on the fault during a representative dynamic rupture. Colorbars indicate the temporal profile on the fault from the beginning of the dynamic rupture. Seismic events cause a sudden increase in pore-fluid pressure, a dynamic stress change, and a drop in viscosity which promotes co-seismic weakening.

the rate-strengthening behavior allows creep to penetrate from both the left and the right segments towards the center of the fault, thus leading to a mechanical erosion of the locked patch. Due to a relatively large critical nucleation size (L_c , Eq. (51)), seismic events nucleate at the center of the seismogenic zone and the resulting dynamic ruptures typically propagate in a bilateral and symmetric fashion (Fig. 4a). For the reference model, the average slip rate is 0.82 m s^{-1} , whereas the average rupture speed is $\sim 2.35 \text{ km s}^{-1}$.

Evolution of the cumulative slip over multiple earthquake cycles is displayed in Fig. 4b. In particular, the accumulation of slip during the inter-seismic periods is represented by gray lines, which are plotted every 4 years, whereas the co-seismic slip is displayed every 0.4 s when the fault slip exceeds the following threshold (V_{th})

$$V_{th} = \frac{2\gamma p_{\text{eff}} c_s}{\mu}, \quad (48)$$

which, according to our parameters, yields to a threshold of 8.1 cm s^{-1} . When the fault is experiencing a seismic event, the cumulative slip on the fault indicates that a complete fault rupture produces $\sim 5 \text{ m}$ of slip, which is followed by a transient post-seismic deformation of $\sim 0.8\text{--}1 \text{ m}$ (blue lines; Fig. 4b). Our models show that dynamic ruptures occur due

to an abrupt increase of pore-fluid pressure within the fault zone (Fig. 5a). The increase in pore-fluid pressure is simultaneously coupled to a rapid decrease in shear strength (Fig. 5b) and both shear and compaction viscosity (Fig. 5c), which are self-sustained by a localized strain rate. When an event begins to propagate dynamically, it produces a shear stress breakdown from its maximum static value to a low, dynamic value (Fig. 5b). Notably, at co-seismic slip rates, the effective shear viscosity drops by roughly 10 orders of magnitude (Fig. 5c), whereas static stress change immediately after the event results in a stress concentration at the transition between the lateral creeping segments and the seismogenic zone.

To investigate the influence that pore-fluid pressure level has on the spontaneous activation of *seismic* and *aseismic* slip on the fault, we perform further numerical experiments in which we increase (model M2) and decrease the effective pressure (p_{eff}) (model M3) compared to the value used for the reference model (Fig. 6). The two models illuminate the effect of pore-fluid pressure throughout the earthquake cycle, from the recurrence period to the nucleation phase of seismic events, as well as the relation between *seismic* and *aseismic* slip. In model M2 (Fig. 6b), due to a lower pore-fluid pressure, the effective pressure on the fault is higher ($p_{\text{eff}} = 60 \text{ MPa}$), and consequently the critical nucleation size decreases. As a result, seismic events nucleate earlier than in the

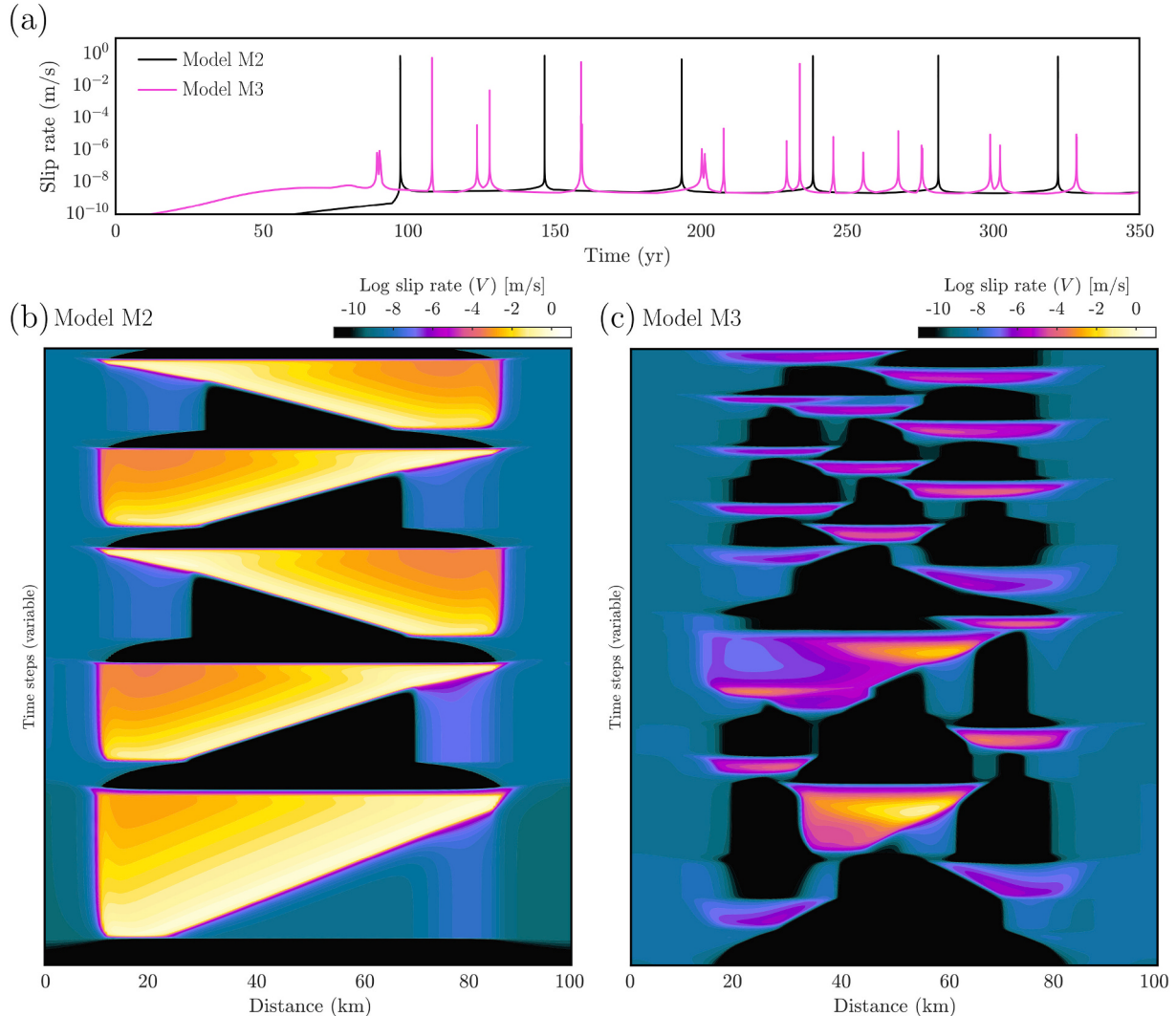


Fig. 6. Overview of the results for the simulations with different effective pressure. (a) Temporal evolution of maximum slip velocity on the fault for models M2 and M3. (b) Model M2 ($p_{\text{eff}} = 60 \text{ MPa}$) is characterized by seismic events of complete ruptures, which propagate asymmetrically from one side of the seismogenic zone to the opposite side. (c) Model M3 ($p_{\text{eff}} = 20 \text{ MPa}$) shows that the same fault segment can regularly slip through slow and fast ruptures, resulting in recurrence intervals that vary over time.

reference model (Fig. 3d). The smaller nucleation size combined with a slightly asymmetric fault structure (Fig. 1b) allow seismic ruptures to nucleate on one side of the seismogenic fault and propagate unilaterally on the other side of the fault segment in an asymmetric fashion. On the other hand, model M3 (Fig. 6c) assumes a higher pore-fluid pressure, which results in a lower effective pressure ($p_{\text{eff}} = 20 \text{ MPa}$). In this case, the average shear strength is significantly lower than in model M2 and plastic yielding occurs more easily. Consequently, the seismogenic zone promotes unstable slip, either as seismic partial ruptures or as slow-slip transients. The long-term slip history indicates a mixture of fast and slow events, with a recurrence interval that vary over time. These results are important, as they suggest that pore-fluid pressure evolution in the same fault segment can release tectonic stress through both slow and fast ruptures, without incorporating any rate- and state-dependent friction.

4. Discussion

4.1. Poro-visco-elasto-plastic (de)compaction and propagation of solitary pressure waves

A large body of theoretical work has explored the physics of solid-fluid interaction in active faults and earthquake source processes (e.g., and references therein Rice and Simons, 1976; Rice, 1992; Segall and Rice, 1995; Garagash and Rudnicki, 2003; Dunham and Rice, 2008; Liu and Rubin, 2010; Miller, 2013). In particular, a number of studies have focused on the relationship between porosity evolution, (de)compaction of reologically complex visco-(elasto)-plastic porous media, and fluid transport through the propagation of porosity waves (e.g., Connolly and Podladchikov, 2000, 2007; Cruz-Atienza et al., 2018, 2018; Yarushina and Podladchikov, 2015; Skarbek and Rempel, 2016; Petrini et al., 2020; Dal Zilio and Gerya, 2022).

According to our results, it appears clear that visco-plastic compaction of fluid-filled porous media can lead to an abrupt self-pressure of the fault zone, particularly under *undrained* conditions or when the permeability on the fault is sufficiently low to prevent fluid flux on the boundaries of the fault zone on the timescale of seismic ruptures. As a result, the self-pressure of the fault zone can trigger the propagation of solitary pressure waves, which can travel at co-seismic speed. To analyze the effect of solid-fluid (de)compaction, we quantify the separate contributions of visco-plastic compaction of the solid skeleton ($\zeta_{[\text{vp}]}$) and the decompaction of the fluid phase ($\zeta_{[\text{el}]}$) as follow:

$$\zeta_{[\text{vp}]} = \frac{p^{[\text{t}]} - p^{[\text{f}]}_{\text{t}}}{\eta^{\phi}(1-\phi)}, \quad (49)$$

$$\zeta_{[\text{el}]} = \frac{\beta^{[\text{d}]}((p^{[\text{t}]}_{\text{t}} - p^{[\text{t}]}_{\text{t}-\Delta_t}) - \alpha(p^{[\text{f}]}_{\text{t}} + p^{[\text{f}]}_{\text{t}-\Delta_t}))}{\Delta_t}. \quad (50)$$

(De)compaction along the fault during a representative major event is shown in Fig. 7. Temporal evolution of the slip velocity displays a large event propagating unilaterally from the left to the right side of the seismogenic zone (Fig. 7a). An accurate quantification of visco-plastic compaction from Eq. (49) and elastic decompaction from Eq. (50) indicates that plastic yielding during the gradual nucleation phase is associated with a rapid increase in solid compaction (Fig. 7b), which is followed by a negative increase of fluid decompaction (Fig. 7c). As a result, pore-fluid pressure on the fault increases while shear strength decreases, thus causing a shear instability. Such shear instability grows on a relatively short time scale, causing the propagation of a dynamic rupture in the form of a pulse-like pressure wave (Fig. 7d). Notably, the strain difference between the elastic decompaction and the visco-plastic compaction represents the finite pore volume change. The combination of these two interconnected processes results in a small change in

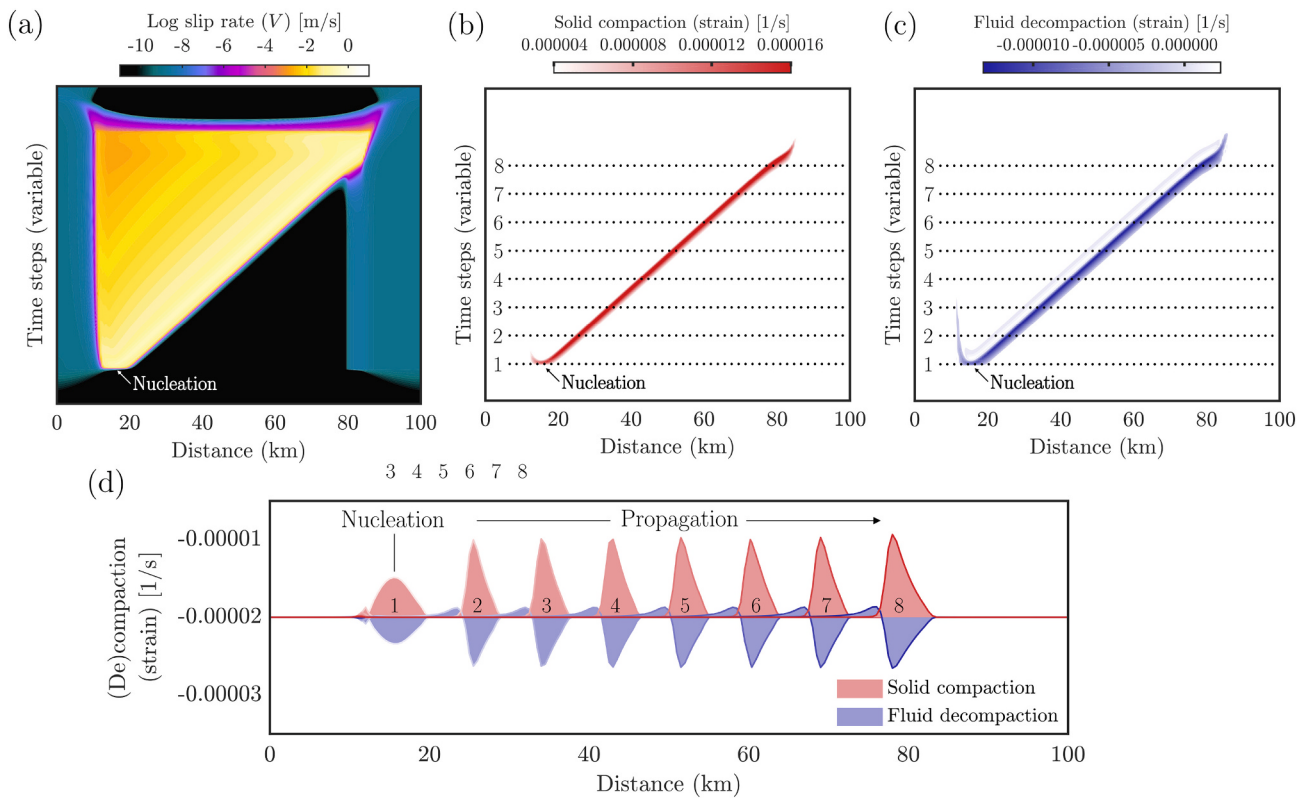


Fig. 7. Compaction vs. decompaction within the fault zone. (a) Temporal evolution of slip rate for a representative major rupture events. (b) Evolution of visco-plastic compaction of the solid skeleton, computed from Eq. (49). (c) Evolution of elastic decompaction of the fluid phase, computed from Eq. (50). (d) Pressure wave propagation due to dynamic rupture, in which the visco-plastic compaction is mirrored by the elastic decompaction. The strain difference between visco-plastic compaction and elastic decompaction are computed from the 8 profiles shown in panel (b) and (c) and they represent the finite pore volume change.

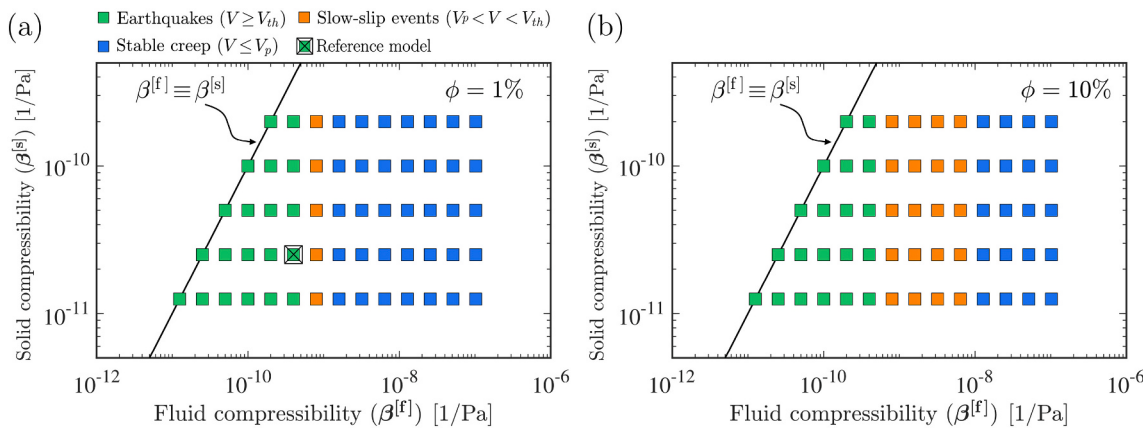


Fig. 8. Impact of solid-fluid compressibility on the slip pattern. (a) Comparison between fluid compressibility ($\beta^{[f]}$) and solid compressibility ($\beta^{[s]}$) assuming a porosity (ϕ) of 1%. (b) Comparison between fluid compressibility and solid compressibility assuming a porosity of 10%. Marker colors indicate the slip response of the fault, ranging from fast regular earthquake to slow-slip events and stable creep.

porosity and, in turn, permeability (Eq. (5)). Furthermore, a dynamic rupture causes an increased in pore-fluid pressure due to elastically stressed pores, which is better resolved by our fully compressible model with rate dependent strength compared to the previous simplified incompressible formulation (Petrini et al., 2020). Such increases in pore-fluid pressure are released over a relatively long diffusion period, which essentially depends on the permeability of both the host rock and the fault zone.

It is important to note that the magnitude of visco-plastic and elastic (de)compaction depend on the compressibility of both the solid skeleton ($\beta^{[s]}$) and the fluid phase ($\beta^{[f]}$), as they have a direct impact on the Biot-Willis coefficient (α ; Eq. (6b)), and the Skempton coefficient (B ; Eq. (6c)). To quantify the role of solid and fluid compressibility, we execute two parameter studies of solid-fluid compressibility assuming two end-member porosities (i.e., 1% and 10%; Tewksbury-Christle and Behr, 2021), knowing that in nature the compressibility of porous rocks, and in particular fluids, can vary up to two orders of magnitude (e.g., Zimmerman et al., 1986; Span and Wagner, 1996; Mitchell and Soga, 2005). Our models produce distinctly different slip patterns within the range of solid-fluid compressibility (Fig. 8). As illustrated in Fig. 8a, an increase in fluid compressibility leads to a transition from regular seismic events, to slow-slip events and eventually stable creep. In contrast, solid compressibility plays only a subordinate role. Furthermore, when we increase the reference porosity from 1% to 10% (Fig. 8b), the parameter space in which we observe slow-slip events broaden. While high porosity

serves as a damping factor to suppress the self-pressurization of pore-fluid and thus the occurrence of fast events, these results indicate that fluid compressibility can significantly affect the slip response of a fault loaded by tectonic stresses. As such, the higher the fluid compressibility, the lower the self-pressurization of the fault zone. Our numerical results can thus reproduce the full spectrum of fault slip behaviors under geophysically relevant conditions of pore-fluid pressure and fault composition, from slow to fast events, as observed for tectonic faults (e.g., Bürgmann, 2018; Obara and Kato, 2016; Jolivet and Frank, 2020).

4.2. Nucleation length, cohesive zone size, and fracture energy

The computational framework presented here is capable of resolving long-term deformation histories with continuous aseismic creep in the stable rate-strengthening fault regions throughout the loading period, nucleation of shear instabilities, co-seismic propagation of seismic ruptures, and post-seismic relaxation. As the considered example shown in Fig. 9, the algorithm is formulated with a rate-strengthening yield strength (Eq. (16)), in which the rate-strengthening exponent (γ) is decisive for its success to reproduce long-term inter-seismic periods with essentially quasi-static deformation, aseismic slip, and most importantly, gradual nucleation of dynamic ruptures (Fig. 9a) (e.g., Dieterich, 1992; Lapusta et al., 2000). However, compared to the formulation of the classical rate- and state-dependent friction laws (e.g., Scholz, 1998),

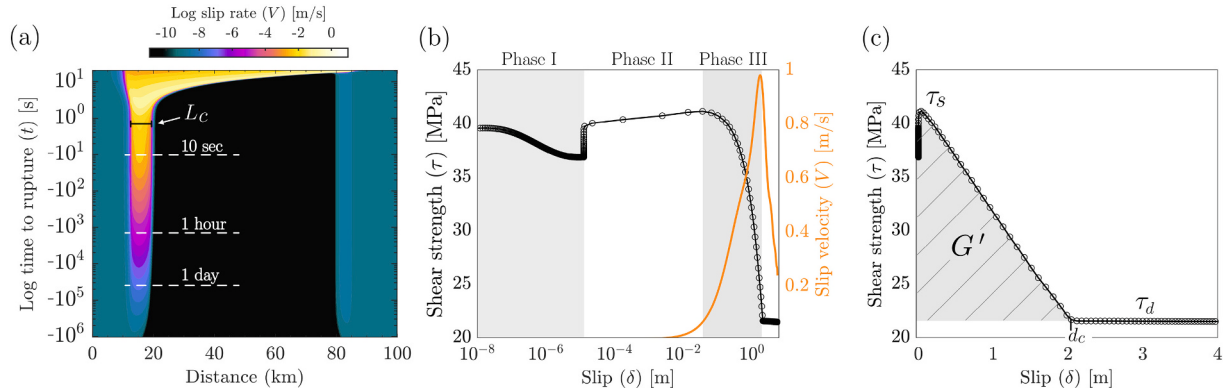


Fig. 9. Nucleation size, slip evolution, and fracture energy. (a) Evolution of slip rate for a representative major event showing the gradual nucleation phase of a dynamic rupture. The y-axis displays time in log-scale. L_c indicates the critical nucleation size (Eq. (51)). (b) Weakening phases measured in the middle of the seismogenic zone ($x = 50$ km). Black line and circles indicate the evolution of shear strength (τ) with the cumulative slip (δ), whereas the orange line displays the evolution of slip rate (V) with the cumulative slip (δ). (c) Shear strength vs. slip. Shear strength linearly decreases from static shear strength (τ_s) to a relatively low dynamic shear strength (τ_d) over a characteristic slip weakening distance (d_c). The gray area illustrate the fracture energy (G') computed from Eq. (53).

the evolutionary effect during the weakening phase is controlled by self-pressurization of pore-fluid pressure.

Our models indicate that shear cracks would become unstable when they reach the critical nucleation length (L_c) proposed by Andrews (1976), in which shear strength linearly decreases from static shear strength (τ_s) to a relatively low dynamic shear strength (τ_d) over a characteristic slip weakening distance (d_c) (Ida, 1972)

$$L_c = \frac{\mu(\tau_s - \tau_d)d_c}{\pi(1-\nu)(\tau_0 - \tau_d)^2} \quad (51)$$

where τ_0 represents the initial shear stress (Eq. (18)). According to our model (Fig. 9a), Eq (51) predicts a critical nucleation length of ~ 7.3 km. Comparing Fig. 4a and Fig. 6a with Fig. 9a, we notice that slip during and right after the nucleation phase are very similar despite the different critical nucleation length. This means that observing signals from the nucleation of fluid-driven shear cracks do not provide any evidence on the final size of the event. This suggests that the final size of seismic events is determined by the conditions on the fault, rather than by the nucleation process itself.

Fig. 9b illustrates the weakening phases that buffer the pore pressure and slip velocity rise, leading to dynamic rupture. During Phase I, upon rapid loading, shear stress rises abruptly with strain as the fault is elastically loaded previous to the onset of slip. Phase II is characterized by a strain-hardening shear strength, which produces an early phase of slip (<1 cm of slip), and corresponds roughly to slip rates of the order of $1\text{--}10$ cm s $^{-1}$. During Phase III, an abrupt weakening is initiated and shear strength drops while slip rate quickly accelerates up to \sim m/s. Peak in slip rate is reached when strength drop is completed, which is followed by a quasi steady-state phase where low shear strength is maintained with minor fluctuations.

During the nucleation phase of a seismic event, slip velocity increases rapidly while shear stress drops significantly. Since the rupture speed during this phase is still close to zero, the critical distance along which the shear stress drops represents the quasi static cohesive zone length (Λ). The cohesive zone size is an important resolution criterion in dynamic rupture because it provides the critical spatial length scale over which the shear stress drops at the propagating rupture front (Palmer and Rice, 1973; Day et al., 2005). Since fluid-driven shear cracks essentially mimic a linear slip-weakening law (Fig. 9c), the cohesive zone sizes at rupture speed $c = 0^+$ (Λ_0) observed in our simulations correspond quite well to the estimate proposed by Day et al. (2005):

$$\Lambda_0 = \frac{9\pi}{32} \frac{\mu^* d_c}{(\tau_s - \tau_d)}, \quad (52)$$

where $9\pi/32$ is a constant if the stress traction distribution within the cohesive zone is linear in space (Palmer and Rice, 1973). This latter study establishes that $\Lambda_0/\Delta x$ of 3 to 5 is required to resolve dynamic rupture. The ratio of nucleation zone size and cohesive zone size (Λ_0/L_c) is between 0.3 and 0.5, as reported in previous studies (e.g., Lapusta et al., 2000). Therefore, resolving the cohesive zone is the most important critical length scale. In our simulations, we choose a cell size of $\Delta x=100$ m, which allows us to resolve the cohesive zone of 2.5 km with at least 25 cells.

Seismic ruptures are controlled by an energy balance involving elastic work, wave radiation, and dissipation by anelastic processes, including friction and plastic strain. As illustrated in Fig. 9c, the frictional work during the weakening process — as the product of shear stress and slip — equates to a simple form of fracture energy (G'), which assumes a linear slip weakening (Palmer and Rice, 1973; Andrews, 1976; Okubo and Dieterich, 1984)

$$G'(\delta) = \int_0^\delta [\tau(\delta') - \tau(\delta)] d\delta' \approx \frac{1}{2}(\tau_s - \tau_d)d_c. \quad (53)$$

To compare our modeling results with existing measurements of fracture energy from earthquakes globally, we compile fracture energy estimates made previously with events spanning five orders of magnitude in size, from borehole microseismicity to great earthquakes (Abercrombie and Rice, 2005; Rice, 2006; Malagnini et al., 2014; Viesca and Garagash, 2015; Nielsen et al., 2016a; Tinti et al., 2005) (Fig. 10). Previous inferences have shown a nonlinear scaling of fracture energy with slip (Abercrombie and Rice, 2005), from $G \propto \delta^2$ for small earthquakes to $G \propto \delta^{2/3}$ for large earthquakes (Fig. 10), which has been attributed to thermal pressurization of pore-fluid by the rapid shear heating of fault gouge (Viesca and Garagash, 2015). For the set of parameters considered in this study, our models produce both relatively large stress drop ($\tau_s - \tau_d$) and large characteristic slip weakening distance (d_c), which results in high values of fracture energy (Fig. 9c). Remarkably, the range of fracture energy and slip from our dynamic analysis supports the observed $G \propto \delta^{2/3}$ scaling of fracture energy for large earthquakes, and suggests that self-pressurization of fluids is a viable mechanism for explaining widespread and prominent process of fault weakening.

It is important to note that in our models d_c is not a constant, as it is treated as variable and it is dynamically determined during rupture itself (Fig. 9c). The weakening distance d_c has been widely used in fault studies and often imposed as a constant (e.g., Tse and Rice, 1986; Ben-Zion and Rice, 1995; Lapusta et al., 2000; Rubin and Ampuero, 2005; Lapusta and Liu, 2009). However, ample observations suggest

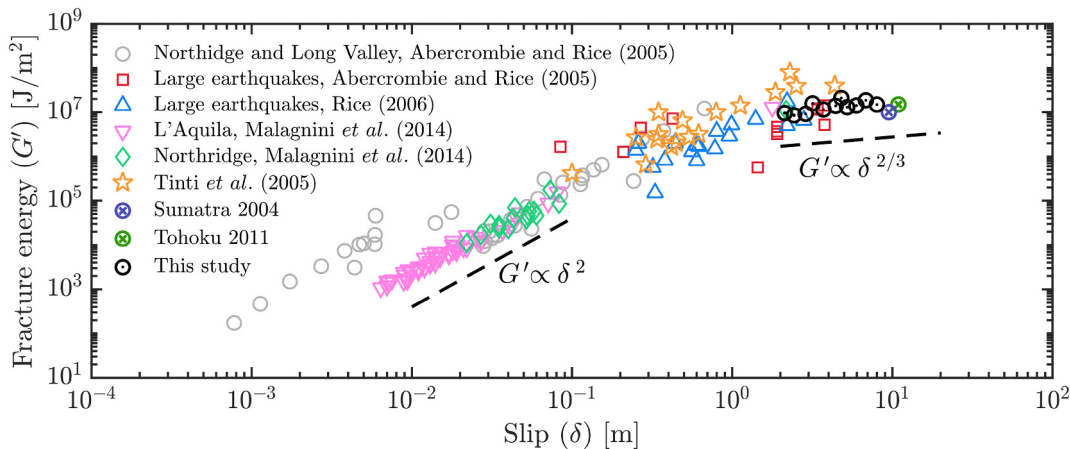


Fig. 10. Compilation of fracture energy (G') and slip (δ) from different earthquakes worldwide, from borehole microseismicity to great earthquakes (Abercrombie and Rice, 2005; Rice, 2006; Malagnini et al., 2014; Viesca and Garagash, 2015; Nielsen et al., 2016a; Tinti et al., 2005). Black dashed lines indicate the different scaling for small ($G \propto \delta^2$) and large ($G \propto \delta^{2/3}$) earthquakes.

that d_c should be treated as a variable (Cocco and Bizzarri, 2002; Nielsen et al., 2010), since the effective weakening distance depends on slip history and loading conditions (e.g., Guatteri et al., 2001; Tinti et al., 2004). Furthermore, laboratory measures of d_c using rotary friction experiments performed at seismic slip rates ($\sim 1 \text{ m s}^{-1}$) yield weakening distances of the order of meters (and references therein Nielsen et al., 2016a), substantial friction drops (Di Toro et al., 2011), and fracture energies arguably in the same order as the seismological estimates (Nielsen et al., 2016b).

4.3. Future avenues for research

Despite the simple setup, the proposed methodology can be used to investigate a number of different problems related to solid-fluid interactions, e.g., fluid-driven swarms, aftershocks, and foreshock sequences (e.g., Ross et al., 2020; Miller, 2020). Furthermore, the developed methodology presents a promising avenue for investigating slip that occurs in response to fluid injection into a permeable fault governed by either rate-strengthening yield strength or rate-and-state friction (e.g., Yang and Dunham, 2021). It is important to note that inelastic changes of permeability and porosity, which can arise from shear-induced dilatancy (e.g., Segall and Rice, 1995), have been neglected for simplicity. Future research will focus on the dynamic evolution of permeability, including deformation-induced changes in pores connectivity and dilatancy effect in a more complex time-dependent hydro-thermo-mechanical framework. However, our results demonstrate that the (de)compaction of the fault zone and associated fluid pressurization are the dominant mechanism controlling the occurrence of fault failure. Shear-induced dilatancy of fault gouge is a transient phenomenon during the initial stages of fault slip, and its effect is poorly constrained at great depth as it is only investigated experimentally at relatively low-pressure conditions (e.g., Brantut et al., 2018). Furthermore, laboratory measurements of pore-fluid pressure variations during fast slip in fault gouge samples seem to confirm that both mechanical compaction and fluid pressurization can overcome the initial phase of shear-induced dilatancy and thus induce fault failure (Aretusini et al., 2021). Future work will also focus on three-dimensional models (e.g., Jiang et al., 2022) and more realistic scenarios of geologic faults (e.g., Dal Zilio et al., 2018, 2019), which will allow to investigate the full spectrum of slip behavior observed in different tectonic settings (e.g., Jolivet and Frank, 2020; Behr and Bürgmann, 2021; Dal Zilio et al., 2021).

While space geodesy has revolutionized our understanding of how tectonic faults accommodate earthquakes, slow-slip transients, and stable creep (e.g., Bürgmann, 2018), their short instrumental record makes it virtually impossible to understand the spatiotemporal interplay between different slip modes. Investigating whether pore-fluid diffusion affects variations in earthquake recurrence intervals, or fault tremor sequences with alternating longer and shorter repeat times (so-called period-doubling events) (Shelly, 2010), is a central question in earthquake physics. Also, systematic investigation of the visco-plastic bulk conditions that control slow-slip events (e.g., Viesca and Dublanchet, 2018; Lambert and Barbot, 2016; Gao and Wang, 2017; Wang and Barbot, 2020; Fagereng, Beall, 2021; Dal Zilio et al., 2022), rather than fault frictional properties (e.g., (Liu and Rice, 2007; Dal Zilio et al., 2020)), is an important frontier in earthquake source modeling. Further implementations can also account for temperature evolution, fault dilation, shear heating, thermal runaway (e.g., Braeck and Podladchikov, 2007), and the evolution of grain size (e.g., Austin and Evans, 2007), which can provide new insights into the onset of highly localized, fine-grained shear processes. Since shear heating can rapidly increase

temperature (Viesca and Garagash, 2015), the associated weakening of shear strength may provide the conditions for episodic slow-slip transients, even under rate-strengthening fault behavior.

5. Conclusions

We have developed a finite difference method to account for fully coupled solid-fluid interaction over many earthquake cycles. The computational framework can model rate-strengthening plasticity in a poro-visco-elasto-plastic rheology. Numerical results are verified through convergence tests and comparisons with analytical benchmarks of pore-fluid pressure diffusion from an injection point along a finite fault width. Future work will include a deeper exploration of parameter space, including the effects of permeability, rate-strengthening, and viscosity, as our set of parameters were chosen primarily for efficiency of computation. For the parameter study in this work, we found that pore-fluid pressure, porosity, and solid-fluid compressibility, influence the occurrence of *seismic* and *aseismic* slip.

We have investigated spontaneously occurring shear instabilities on a mildly rate-strengthening fault zone with solid-fluid coupling. Remarkably, these instabilities are fundamentally different from standard instabilities with rate-and-state friction in that they are controlled by localized (de)compaction of pores and dynamic self-pressurization of fluids inside the undrained fault zone. Simulations show that these fluid-driven dynamic ruptures are controlled by solitary pulse-like pressure waves propagating at seismic speed. We have proposed a conceptual model for how this type of instability manifest in a 2-D plane strain shear model (mode-II). However, we recognize that in order to make a full comparison to geological settings we need to understand how the reported instabilities manifest in three dimensions. Despite this limitation, our work demonstrates how pore-fluid pressure, poroelastic effects, and inelastic deformation, can destabilize active faults and produce the full spectrum of slip, from fast- to slow-slip, consistent with observations.

Although multiple weakening mechanisms may operate on active faults, our results suggest that self-pressurization of fluid-filled porous rocks may be the dominant contributor to fault fracture energy, particularly for large earthquakes. Understanding how faults lose their shear strength during fluid-induced dynamic rupture is critical, as it may help to constrain the minimum level of shear stress a fault requires to become unstable. In a broader context, this study shows the importance of incorporating the realistic hydro-mechanical structure of faults to investigate sequences of *seismic* and *aseismic* slip. In particular, this study indicates that pore-pressure evolution can completely change both the failure process on the interface and the long-term slip history of geologic faults.

Data availability statement

Data related to this paper are stored in the ETH-Bibliothek and can be downloaded from the following link: <http://hdl.handle.net/20.500.11850/532225> (doi: <http://10.3929/ethz-b-000532225>)

Declaration of Competing Interest

The authors declare that they have no known competing financial interests or personal relationships that could have appeared to influence the work reported in this paper.

Data availability

No data was used for the research described in the article.

Acknowledgments

We thank Nadia Lapusta, Massimo Cocco, Paul Selvadurai, Claudio Petrini, Elias Heimisson, Federico Ciardo, Domenico Giardini, and Casper Pranger for discussions. This research was supported by the

European Research Council (ERC) Synergy Grant FEAR (ID: 856559). Numerical simulations were performed on ETH cluster Euler. We thank three anonymous reviewers for their constructive comments, which helped improve the paper considerably.

Appendix A. Discretization of the governing equations

The governing Eqs. (1)–(4) are discretized on a 2-D staggered-grid, which is defined by quadrilaterals cells parallel to the coordinate in x - and y -direction (Fig. A.11). Fig. A.12 shows the stencils used to discretize in 2-D the total momentum (solid matrix and fluid; Eq. (1)) under plane strain conditions ($v_z = 0$) for x - and y -components by including Eqs. (11) and (22a):

$$\begin{aligned} & \left(\frac{\eta_{[xx]}^*(i,j+1)}{\Delta x^2} (v_{x(i,j+1)}^{[s]} - v_{x(i,j)}^{[s]}) - \frac{\eta_{[xx]}^*(i,j)}{\Delta x^2} (v_{x(i,j)}^{[s]} - v_{x(i,j-1)}^{[s]}) \right) \dots \\ & - \left(\frac{\eta_{[xx]}^*(i,j+1)}{\Delta x \Delta y} (v_{y(i,j+1)}^{[s]} - v_{y(i-1,j+1)}^{[s]}) - \frac{\eta_{[xx]}^*(i,j)}{\Delta x \Delta y} (v_{y(i,j)}^{[s]} - v_{y(i-1,j)}^{[s]}) \right) \dots \\ & + \left(\frac{\eta_{[xy]}^*(i,j)}{\Delta y^2} (v_{x(i+1,j)}^{[s]} - v_{x(i,j)}^{[s]}) - \frac{\eta_{[xy]}^*(i-1,j)}{\Delta y^2} (v_{x(i,j)}^{[s]} - v_{x(i-1,j)}^{[s]}) \right) \dots \end{aligned} \quad (\text{A.1})$$

$$\begin{aligned} & + \left(\frac{\eta_{[xy]}^*(i,j)}{\Delta y \Delta x} (v_{y(i,j+1)}^{[s]} - v_{y(i,j)}^{[s]}) - \frac{\eta_{[xy]}^*(i-1,j)}{\Delta y \Delta x} (v_{y(i-1,j+1)}^{[s]} - v_{y(i-1,j)}^{[s]}) \right) - \frac{p_{(i,j+1)}^{[t]} - p_{(i,j)}^{[t]}}{\Delta x} + \rho^{[t]} g_x \\ & = \rho^{[t]} \frac{v_{x(i,j)}^{[s]} - v_{x(i,j)}^{[s]}|_{t-\Delta t}}{\Delta t} - \left(\frac{\tau_{xx}^*(i,j+1) - \tau_{xx}^*(i,j)}{\Delta x} \right) - \left(\frac{\tau_{xy}^*(i,j) - \tau_{xy}^*(i-1,j)}{\Delta y} \right) \end{aligned}$$

$$\begin{aligned} & \left(\frac{\eta_{[yy]}^*(i+1,j)}{\Delta y^2} (v_{y(i+1,j)}^{[s]} - v_{y(i,j)}^{[s]}) - \frac{\eta_{[yy]}^*(i,j)}{\Delta y^2} (v_{y(i,j)}^{[s]} - v_{y(i-1,j)}^{[s]}) \right) \dots \\ & - \left(\frac{\eta_{[yy]}^*(i+1,j)}{\Delta y \Delta x} (v_{x(i+1,j)}^{[s]} - v_{x(i+1,j-1)}^{[s]}) - \frac{\eta_{[yy]}^*(i,j)}{\Delta y \Delta x} (v_{x(i,j)}^{[s]} - v_{x(i,j-1)}^{[s]}) \right) \dots \\ & + \left(\frac{\eta_{[xy]}^*(i,j)}{\Delta x \Delta y} (v_{x(i+1,j)}^{[s]} - v_{x(i,j)}^{[s]}) - \frac{\eta_{[xy]}^*(i,j-1)}{\Delta x \Delta y} (v_{x(i,j-1)}^{[s]} - v_{x(i,j)}^{[s]}) \right) \dots \end{aligned} \quad (\text{A.2})$$

$$\begin{aligned} & + \left(\frac{\eta_{[xy]}^*(i,j)}{\Delta x^2} (v_{y(i,j+1)}^{[s]} - v_{y(i,j)}^{[s]}) - \frac{\eta_{[xy]}^*(i,j-1)}{\Delta x^2} (v_{y(i,j-1)}^{[s]} - v_{y(i,j)}^{[s]}) \right) - \frac{p_{(i+1,j)}^{[t]} - p_{(i,j)}^{[t]}}{\Delta y} + \rho^{[t]} g_y \\ & = \rho^{[t]} \frac{v_{y(i,j)}^{[s]} - v_{y(i,j)}^{[s]}|_{t-\Delta t}}{\Delta t} - \left(\frac{\tau_{yy}^*(i,j+1) - \tau_{yy}^*(i,j)}{\Delta y} \right) - \left(\frac{\tau_{xy}^*(i,j) - \tau_{xy}^*(i,j-1)}{\Delta x} \right) \end{aligned}$$

where $\eta^* = \eta_{vp} Z$, $\tau^* = \tau(1 - Z)$.

Fig. A.13a,b displays the stencils used to discretize the Darcy Eq. (2), whereas Fig. A.13c,d shows the stencils used to discretize the fully compressible solid mass (Eq. (3)) and the fully compressible fluid mass (Eq. (A.6)), respectively:

$$v_x(i,j)^{[\mathrm{D}]} = -\frac{k_{(i,j)}^{[\phi]} (p_{(i,j+1)}^{[\mathrm{f}]} - p_{(i,j)}^{[\mathrm{f}]})}{\eta_{(i,j)}^{[\mathrm{f}]} \Delta x} - \rho^{[\mathrm{f}]} (g_x - \frac{v_{x(i,j)}^{[\mathrm{f}]} - v_{x(i,j)}^{[\mathrm{f}]}|_{t-\Delta t}}{\Delta t}) \quad (\text{A.3})$$

$$v_y(i,j)^{[\mathrm{D}]} = -\frac{k_{(i,j)}^{[\phi]} (p_{(i+1,j)}^{[\mathrm{f}]} - p_{(i,j)}^{[\mathrm{f}]})}{\eta_{(i,j)}^{[\mathrm{f}]} \Delta y} - \rho^{[\mathrm{f}]} (g_y - \frac{v_{y(i,j)}^{[\mathrm{f}]} - v_{y(i,j)}^{[\mathrm{f}]}|_{t-\Delta t}}{\Delta t}) \quad (\text{A.4})$$

$$\begin{aligned} & \left(\frac{(v_{x(i,j)}^{[s]} - v_{x(i,j-1)}^{[s]})}{\Delta x} + \frac{(v_{y(i,j)}^{[s]} - v_{y(i-1,j)}^{[s]})}{\Delta y} \right) \dots \\ & = -\frac{1}{K_{(i,j)}^{[\mathrm{d}]} \Delta t} (p_{(i,j)}^{[\mathrm{t}]} - p_{(i,j)}^{[\mathrm{t}]}|_{t-\Delta t} - \alpha_{(i,j)} \frac{p_{(i,j)}^{[\mathrm{f}]} - p_{(i,j)}^{[\mathrm{f}]}|_{t-\Delta t}}{\Delta t}) - \frac{p_{(i,j)}^{[\mathrm{t}]} - p_{(i,j)}^{[\mathrm{f}]}|_{t-\Delta t}}{\eta_{(i,j)}^{[\phi]} (1 - \phi_{(i,j)})} \end{aligned} \quad (\text{A.5})$$

$$\begin{aligned} & \left(\frac{(v_{x(i,j)}^{[\mathrm{D}]} - v_{x(i,j-1)}^{[\mathrm{D}]})}{\Delta x} + \frac{(v_{y(i,j)}^{[\mathrm{D}]} - v_{y(i-1,j)}^{[\mathrm{D}]})}{\Delta y} \right) \dots \\ & = \frac{\alpha_{(i,j)} (p_{(i,j)}^{[\mathrm{t}]} - p_{(i,j)}^{[\mathrm{t}]}|_{t-\Delta t})}{K_{(i,j)}^{[\mathrm{d}]} \Delta t} - \frac{1}{B_{(i,j)} \Delta t} (p_{(i,j)}^{[\mathrm{f}]} - p_{(i,j)}^{[\mathrm{f}]}|_{t-\Delta t}) + \frac{p_{(i,j)}^{[\mathrm{t}]} - p_{(i,j)}^{[\mathrm{f}]}|_{t-\Delta t}}{\eta_{(i,j)}^{[\phi]} (1 - \phi_{(i,j)})} \end{aligned} \quad (\text{A.6})$$

In order to simulate large displacement of different lithologies, we combine the Eulerian grid with Lagrangian particles (i.e., material points). For each of these particles, we assign the physical properties of the rock types (e.g., viscosity, density, shear modulus, etc.) and, during the evolution of the model, these markers store other properties such as pressure, deviatoric stresses, and velocities. Over time, Lagrangian particles move to their new position following a 4-th order Runge-Kutta scheme, and stresses are rotated according to the vorticity field. At the beginning of each time step, Lagrangian markers are interpolated to the Eulerian grid using a distance-dependent bi-linear interpolation scheme, whereas markers are updated at the end of each time step.

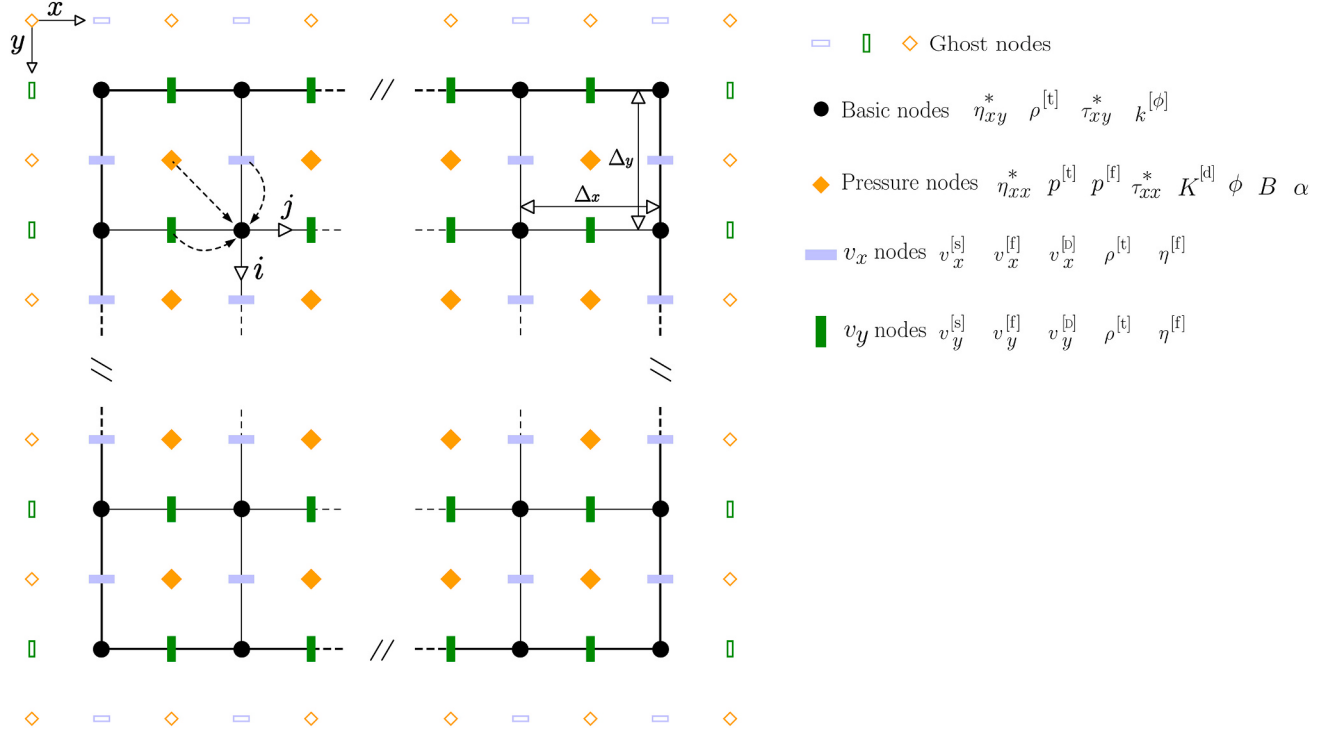


Fig. A.11. Fully staggered grid with representation of the different nodes. The ghost nodes are not used to solve the governing equations and boundary conditions. Different node symbols and colors illustrate the distribution of variables on the staggered nodes.

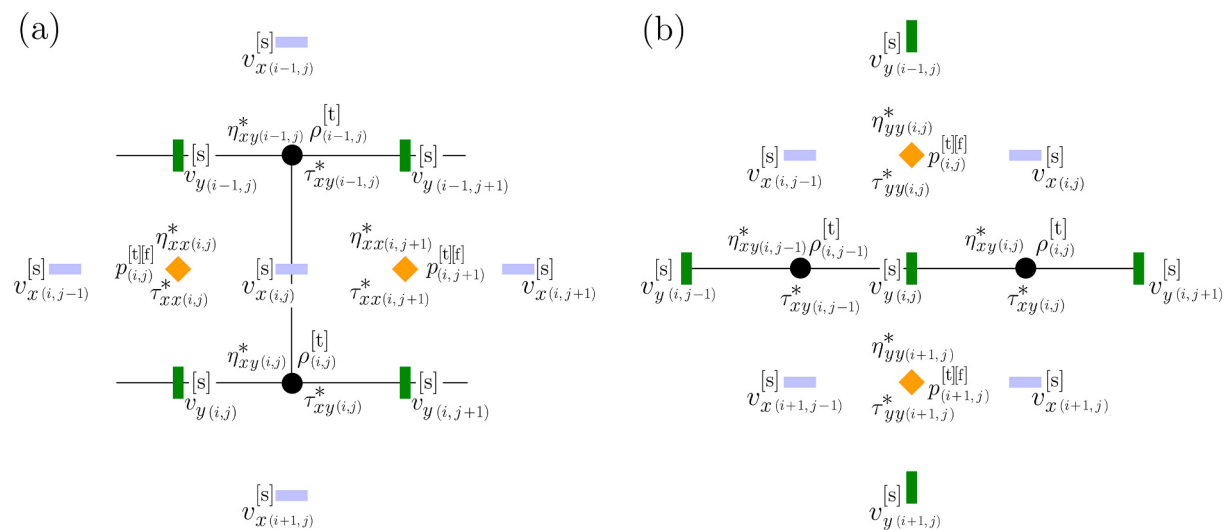


Fig. A.12. Staggered-grid stencils used by our scheme to discretize the total momentum (solid matrix and fluid; Eq. (1)) for x - and y -components.

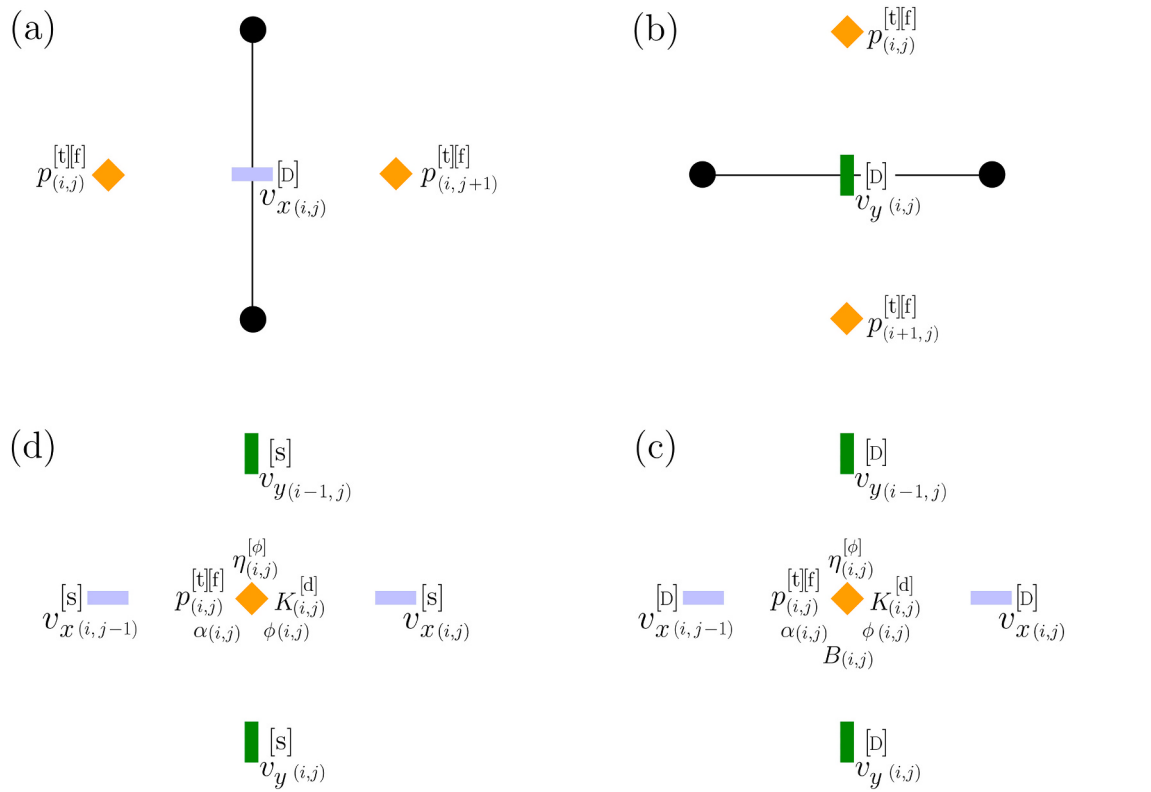


Fig. A.13. Stencils used for discretizing the Darcy equations: (a) x-Darcy equation and (b) y-Darcy equation (Eq. (2)). Stencils used for discretizing the conservation equations: (c) solid mass (Eq. (3)) and (d) fluid mass (Eq. (4)).

References

- Abercrombie, R.E., Rice, J.R., 2005. Can observations of earthquake scaling constrain slip weakening? *Geophys. J. Int.* 162 (2), 406–424.
- Andrews, D., 1976. Rupture velocity of plane strain shear cracks. *J. Geophys. Res.* 81 (32), 5679–5687.
- Aretusini, S., Meneghini, F., Spagnuolo, E., Harbord, C., Di Toro, G., 2021. Fluid pressurisation and earthquake propagation in the hikurangi subduction zone. *Nat. Commun.* 12 (1), 1–8.
- Austin, N.J., Evans, B., 2007. Paleowattmeters: a scaling relation for dynamically recrystallized grain size. *Geology* 35 (4), 343–346.
- Bao, X., Eaton, D.W., 2016. Fault activation by hydraulic fracturing in western Canada. *Science* 354 (6318), 1406–1409.
- Behr, W.M., Bürgmann, R., 2021. What's down there?. The structures, materials and environment of deep-seated slow slip and tremor. *Philosoph. Trans. Royal Soc. A* 379 (2193), 20200218.
- Ben-Zion, Y., Rice, J.R., 1995. Slip patterns and earthquake populations along different classes of faults in elastic solids. *J. Geophys. Res.: Solid Earth* 100 (B7), 12959–12983.
- Bhattacharya, P., Viesca, R.C., 2019. Fluid-induced aseismic fault slip outpaces pore-fluid migration. *Science* 364 (6439), 464–468.
- Biot, M.A., 1941. General theory of three-dimensional consolidation. *J. Appl. Phys.* 12 (2), 155–164.
- Biot, M.A., Willis, D.G., 1957. The Elastic Coefficients of the Theory of Consolidation.
- Bishop, A., 1973. The influence of an undrained change in stress on the pore pressure in porous media of low compressibility. *Geotechnique* 23 (3), 435–442.
- Braeck, S., Podladchikov, Y., 2007. Spontaneous thermal runaway as an ultimate failure mechanism of materials. *Phys. Rev. Lett.* 98 (9), 095504.
- Brantut, N., Baker, M., Hansen, L.N., Baud, P., 2018. Microstructural control of physical properties during deformation of porous limestone. *J. Geophys. Res.: Solid Earth* 123 (6), 4751–4764.
- Bürgmann, R., 2018. The geophysics, geology and mechanics of slow fault slip. *Earth Planet. Sci. Lett.* 495, 112–134.
- Cappa, F., Guglielmi, Y., Nussbaum, C., Birkholzer, J., 2018. On the relationship between fault permeability increases, induced stress perturbation, and the growth of aseismic slip during fluid injection. *Geophys. Res. Lett.* 45 (20), 11–012.
- Carslaw, H.S., Jaeger, J.C., 1959. Conduction of Heat in Solids. Technical Report. Clarendon Press, Oxford, United Kingdom.
- Chen, X., Shearer, P., Abercrombie, R., 2012. Spatial migration of earthquakes within seismic clusters in southern California: evidence for fluid diffusion. *J. Geophys. Res.: Solid Earth* 117 (B4).
- Cocco, M., Bizzarri, A., 2002. On the slip-weakening behavior of rate-and state dependent constitutive laws. *Geophys. Res. Lett.* 29 (11), 11–21.
- Connolly, J., Podladchikov, Y.Y., 2000. Temperature-dependent viscoelastic compaction and compartmentalization in sedimentary basins. *Tectonophysics* 324 (3), 137–168.
- Connolly, J., Podladchikov, Y.Y., 2007. Decompression weakening and channeling instability in ductile porous media: implications for asthenospheric melt segregation. *J. Geophys. Res.: Solid Earth* 112 (B10).
- Cruz-Atienza, V.M., Villafuerte, C., Bhat, H.S., 2018. Rapid tremor migration and pore-pressure waves in subduction zones. *Nat. Commun.* 9 (1), 1–13.
- Dal Zilio, L., Gerya, T., 2022. Subduction earthquake cycles controlled by episodic fluid pressure cycling. *Lithos* 426–427, 106800.
- Dal Zilio, L., Hetényi, G., Hubbard, J., Bollinger, L., 2021. Building the Himalaya from tectonic to earthquake scales. *Nat. Rev. Earth Environ.* 2, 251–268.
- Dal Zilio, L., Lapusta, N., Avouac, J.-P., Gerya, T., 2020. Unraveling scaling properties of slow-slip events. *Geophys. Res. Lett.* 47 (10).
- Dal Zilio, L., Lapusta, N., Avouac, J.-P., Gerya, T., 2022. Subduction earthquake sequences in a nonlinear visco-elasto-plastic megathrust. *Geophys. J. Int.* 229 (2), 1098–1121.
- Dal Zilio, L., van Dinther, Y., Gerya, T., Avouac, J.-P., 2019. Bimodal seismicity in the Himalaya controlled by fault friction and geometry. *Nat. Commun.* 10 (1), 48.
- Dal Zilio, L., van Dinther, Y., Gerya, T.V., Pranger, C.C., 2018. Seismic behaviour of mountain belts controlled by plate convergence rate. *Earth Planet. Sci. Lett.* 482, 81–92.
- Day, S.M., Dalguer, L.A., Lapusta, N., Liu, Y., 2005. Comparison of finite difference and boundary integral solutions to three-dimensional spontaneous rupture. *J. Geophys. Res.: Solid Earth* 110 (B12).
- Deichmann, N., Giardini, D., 2009. Earthquakes induced by the stimulation of an enhanced geothermal system below Basel (Switzerland). *Seismol. Res. Lett.* 80 (5), 784–798.
- Di Toro, G., Han, R., Hirose, T., De Paola, N., Nielsen, S., Mizoguchi, K., Ferri, F., Cocco, M., Shimamoto, T., 2011. Fault lubrication during earthquakes. *Nature* 471 (7339), 494–498.
- Dieterich, J., 1981. Constitutive Properties of Faults with Simulated Gouge Monograph 24: Mechanical Behavior of Crustal Rocks. Washington, DC: American Geophysical Union, pp. 103–120.
- Dieterich, J.H., 1979. Modeling of rock friction: 1. experimental results and constitutive equations. *J. Geophys. Res.: Solid Earth* 84 (B5), 2161–2168.
- Dieterich, J.H., 1992. Earthquake nucleation on faults with rate-and state-dependent strength. *Tectonophysics* 211 (1–4), 115–134.
- Dublanchet, P., 2019. Fluid driven shear cracks on a strengthening rate-and-state frictional fault. *J. Mech. Phys. Solids* 132, 103672.

- Dunham, E.M., Rice, J.R., 2008. Earthquake slip between dissimilar poroelastic materials. *J. Geophys. Res.: Solid Earth* 113 (B9).
- Ellsworth, W.L., 2013. Injection-induced earthquakes. *Science* 341, 6142.
- Ellsworth, W.L., Giardini, D., Townend, J., Ge, S., Shimamoto, T., 2019. Triggering of the Pohang Korea, earthquake (Mw 5.5) by enhanced geothermal system stimulation. *Seismol. Res. Lett.* 90 (5), 1844–1858.
- Fagereng, Å., Beall, A., 2021. Is complex fault zone behaviour a reflection of rheological heterogeneity? *Philosoph. Trans. Royal Soc. A* 379 (2193), 20190421.
- Gao, X., Wang, K., 2017. Rheological separation of the megathrust seismogenic zone and episodic tremor and slip. *Nature* 543 (7645), 416.
- Garagash, D.I., Germanovich, L.N., 2012. Nucleation and arrest of dynamic slip on a pressurized fault. *J. Geophys. Res.: Solid Earth* 117 (B10).
- Garagash, D.I., Rudnicki, J.W., 2003. Shear heating of a fluid-saturated slip-weakening dilatant fault zone 1. limiting regimes. *J. Geophys. Res.: Solid Earth* 108 (B2).
- Gassmann, F., 1951. Elastic waves through a packing of spheres. *Geophysics* 16 (4), 673–685.
- Gerya, T., 2019. Introduction to Numerical Geodynamic Modelling. Cambridge University Press.
- Gerya, T., Yuen, D., 2007. Robust characteristics method for modelling multiphase visco-elasto-plastic thermo-mechanical problems. *Phys. Earth Planetary Interiors* 163 (1), 83–105.
- Grigoli, F., Cesca, S., Priolo, E., Rinaldi, A.P., Clinton, J.F., Stabile, T.A., Dost, B., Fernandez, M.G., Wiemer, S., Dahm, T., 2017. Current challenges in monitoring, discrimination, and management of induced seismicity related to underground industrial activities: a European perspective. *Rev. Geophys.* 55 (2), 310–340.
- Guatteri, M., Spudich, P., Beroza, G.C., 2001. Inferring rate and state friction parameters from a rupture model of the 1995 Hyogo-Ken Nanbu (Kobe) Japan earthquake. *J. Geophys. Res.: Solid Earth* 106 (B11), 26511–26521.
- Guglielmi, Y., Cappa, F., Avouac, J.-P., Henry, P., Ellsworth, D., 2015. Seismicity triggered by fluid injection-induced aseismic slip. *Science* 348 (6240), 1224–1226.
- Hainzl, S., 2004. Seismicity patterns of earthquake swarms due to fluid intrusion and stress triggering. *Geophys. J. Int.* 159 (3), 1090–1096.
- Hatch, R.L., Abercrombie, R.E., Ruhl, C.J., Smith, K.D., 2020. Evidence of aseismic and fluid-driven processes in a small complex seismic swarm near Virginia City, Nevada. *Geophys. Res. Lett.* 47 (4) e2019GL085477.
- Heimisson, E.R., Dunham, E.M., Almqvist, M., 2019. Poroelastic effects destabilize mildly rate-strengthening friction to generate stable slow slip pulses. *J. Mech. Phys. Solids* 130, 262–279.
- Herrendörfer, R., 2018. Modeling of the Slip Spectrum Along Mature and Spontaneously Forming Faults in a Visco-Elasto-Plastic Continuum. ETH Zurich. PhD thesis.
- Ida, Y., 1972. Cohesive force across the tip of a longitudinal-shear crack and griffith's specific surface energy. *J. Geophys. Res.* 77 (20), 3796–3805.
- Jiang, J., Erickson, B., Lambert, V., Ampuero, J.-P., Ando, R., Barbot, S., Cattania, C., Dal Zilio, L., Duan, B., Dunham, E.M., Gabriel, A.-A., Lapusta, N., Li, D., Liu, D., Liu, Y., Ozawa, S., Pranger, C., Van Dinther, Y., 2022. Community-driven code comparisons for three-dimensional dynamic modeling of sequences of earthquakes and aseismic slip (seas). *J. Geophys. Res.: Solid Earth* 127 (3).
- Jolivet, R., Frank, W., 2022. The transient and intermittent nature of slow slip. *AGU Adv.* 1 (1) e2019AV000126.
- Katz, R.F., Spiegelman, M., Holtzman, B., 2006. The dynamics of melt and shear localization in partially molten aggregates. *Nature* 442 (7103), 676–679.
- Keranen, K.M., Savage, H.M., Abers, G.A., Cochran, E.S., 2013. Potentially induced earthquakes in Oklahoma USA: links between wastewater injection and the 2011 Mw 5.7 earthquake sequence. *Geology* 41 (6), 699–702.
- Keranen, K.M., Weingarten, M., Abers, G.A., Bekins, B.A., Ge, S., 2014. Sharp increase in central Oklahoma seismicity since 2008 induced by massive wastewater injection. *Science* 345 (6195), 448–451.
- Lambert, V., Barbot, S., 2016. Contribution of viscoelastic flow in earthquake cycles within the lithosphere-asthenosphere system. *Geophys. Res. Lett.* 43 (19), 10–142.
- Lapusta, N., Liu, Y., 2009. Three-dimensional boundary integral modeling of spontaneous earthquake sequences and aseismic slip. *J. Geophys. Res.: Solid Earth* 114 (B9).
- Lapusta, N., Rice, J.R., Ben-Zion, Y., Zheng, G., 2000. Elastodynamic analysis for slow tectonic loading with spontaneous rupture episodes on faults with rate-and state-dependent friction. *J. Geophys. Res.: Solid Earth* 105 (B10), 23765–23789.
- Larochelle, S., Lapusta, N., Ampuero, J.-P., Cappa, F., 2021. Constraining fault friction and stability with fluid-injection field experiments. *Geophys. Res. Lett.* 48 e2020GL091188.
- Liu, Y., Rice, J.R., 2007. Spontaneous and triggered aseismic deformation transients in a subduction fault model. *J. Geophys. Res.: Solid Earth* 112 (B9).
- Liu, Y., Rubin, A.M., 2010. Role of fault gouge dilatancy on aseismic deformation transients. *J. Geophys. Res.: Solid Earth* 115 (B10).
- Malagnini, L., Cocco, M., Nielsen, S., Mayeda, K., Boschi, E., et al., 2014. Gradual fault weakening with seismic slip: inferences from the seismic sequences of L'Aquila, 2009, and Northridge, 1994. *Pure Appl. Geophys.* 171 (10), 2709–2730.
- Marone, C., 1998. Laboratory-derived friction laws and their application to seismic faulting. *Annu. Rev. Earth Planet. Sci.* 26 (1), 643–696.
- Miller, S.A., 2013. The role of fluids in tectonic and earthquake processes. *Adv. Geophys.* 54, 1–46. Elsevier.
- Miller, S.A., 2020. Aftershocks are fluid-driven and decay rates controlled by permeability dynamics. *Nat. Commun.* 11 (1), 1–11.
- Miller, S.A., Collettini, C., Chiaramonte, L., Cocco, M., Barchi, M., Kaus, B.J., 2004. Aftershocks driven by a high-pressure CO₂ source at depth. *Nature* 427 (6976), 724–727.
- Mitchell, J.K., Soga, K., 2005. Fundamentals of Soil Behavior, Volume 3. John Wiley & Sons New York.
- Moresi, L., Dufour, F., Mühlhaus, H.-B., 2003. A lagrangian integration point finite element method for large deformation modeling of viscoelastic geomaterials. *J. Comut. Phys.* 184 (2), 476–497.
- Nielsen, S., Mosca, P., Giberti, G., Di Toro, G., Hirose, T., Shimamoto, T., 2010. On the transient behavior of frictional melt during seismic slip. *J. Geophys. Res.: Solid Earth* 115 (B10).
- Nielsen, S., Spagnuolo, E., Smith, S., Violay, M., Di Toro, G., Bistacchi, A., 2016a. Scaling in natural and laboratory earthquakes. *Geophys. Res. Lett.* 43 (4), 1504–1510.
- Nielsen, S., Spagnuolo, E., Violay, M., Smith, S., Di Toro, G., Bistacchi, A., 2016b. G: fracture energy, friction and dissipation in earthquakes. *J. Seismol.* 20 (4), 1187–1205.
- Nur, A., Booker, J.R., 1972. Aftershocks caused by pore fluid flow? *Science* 175 (4024), 885–887.
- Obara, K., Kato, A., 2016. Connecting slow earthquakes to huge earthquakes. *Science* 353 (6296), 253–257.
- Okubo, P.G., Dieterich, J.H., 1984. Effects of physical fault properties on frictional instabilities produced on simulated faults. *J. Geophys. Res.: Solid Earth* 89 (B7), 5817–5827.
- Palmer, A.C., Rice, J.R., 1973. The growth of slip surfaces in the progressive failure of over-consolidated clay. *Proceedings of the royal society of London. A. Math. Phys. Sci.* 332 (1591), 527–548.
- Peacock, S.M., Christensen, N.I., Bostock, M.G., Audet, P., 2011. High pore pressures and porosity at 35 km depth in the Cascadia subduction zone. *Geology* 39 (5), 471–474.
- Petrini, C., Gerya, T., Yarushina, V., van Dinther, Y., Connolly, J., Madonna, C., 2020. Seismo-hydro-mechanical modelling of the seismic cycle: methodology and implications for subduction zone seismicity. *Tectonophysics* 791, 228504.
- Prager, W., Drucker, D., 1952. Soil mechanics and plastic analysis or limit design. *Quat. Appl.* 10 (2), 157–165.
- Raleigh, C., Healy, J., Bredehoeft, J., 1976. An experiment in earthquake control at Rangely, Colorado. *Sci.* 191 (4233), 1230–1237.
- Rice, J.R., 1992. Fault stress states, pore pressure distributions, and the weakness of the San Andreas fault. *Int. Geophys.* 51, 475–503. Elsevier.
- Rice, J.R., 2006. Heating and weakening of faults during earthquake slip. *J. Geophys. Res.: Solid Earth* 111 (B5).
- Rice, J.R., Cleary, M.P., 1976. Some basic stress diffusion solutions for fluid-saturated elastic porous media with compressible constituents. *Rev. Geophys.* 14 (2), 227–241.
- Rice, J.R., Simons, D.A., 1976. The stabilization of spreading shear faults by coupled deformation-diffusion effects in fluid-infiltrated porous materials. *J. Geophys. Res.* 81 (29), 5322–5334.
- Roland, E., McGuire, J.J., 2009. Earthquake swarms on transform faults. *Geophys. J. Int.* 178 (3), 1677–1690.
- Ross, Z.E., Cochran, E.S., Trugman, D.T., Smith, J.D., 2020. 3D fault architecture controls the dynamism of earthquake swarms. *Science* 368 (6497), 1357–1361.
- Ross, Z.E., Rollins, C., Cochran, E.S., Hauksson, E., Avouac, J.-P., Ben-Zion, Y., 2017. Aftershocks driven by afterslip and fluid pressure sweeping through a fault-fracture mesh. *Geophys. Res. Lett.* 44 (16), 8260–8267.
- Rubin, A.M., Ampuero, J.-P., 2005. Earthquake nucleation on (aging) rate and state faults. *J. Geophys. Res.: Solid Earth* 110 (B11).
- Rubin, A.M., Ampuero, J.-P., 2007. Aftershock asymmetry on a bimaterial interface. *J. Geophys. Res.: Solid Earth* 112 (B5).
- Rudnicki, J.W., Rice, J.R., 2006. Effective normal stress alteration due to pore pressure changes induced by dynamic slip propagation on a plane between dissimilar materials. *J. Geophys. Res.: Solid Earth* 111 (B10).
- Ruina, A., 1983. Slip instability and state variable friction laws. *J. Geophys. Res.: Solid Earth* 88 (B12), 10359–10370.
- Schmalholz, S., Podladchikov, Y., Schmid, D., 2001. A spectral/finite difference method for simulating large deformations of heterogeneous, viscoelastic materials. *Geophys. J. Int.* 145 (1), 199–208.
- Scholz, C.H., 1998. Earthquakes and friction laws. *Nature* 391 (6662), 37–42.
- Segall, P., Rice, J.R., 1995. Dilatancy, compaction, and slip instability of a fluid-infiltrated fault. *J. Geophys. Res.: Solid Earth* 100 (B11), 22155–22171.
- Shelly, D.R., 2010. Periodic, chaotic, and doubled earthquake recurrence intervals on the deep San Andreas fault. *Science* 328 (5984), 1385–1388.
- Skarbek, R.M., Rempel, A.W., 2016. Dehydration-induced porosity waves and episodic tremor and slip. *Geochem. Geophys. Geosyst.* 17 (2), 442–469.
- Skepton, A.W., 1960. Effective Stress in Soils, Concrete, and Rock In Pore Pressure and Suction in Soils. Butterworths, London, pp. 4–16.
- Span, R., Wagner, W., 1996. A new equation of state for carbon dioxide covering the fluid region from the triple-point temperature to 1100 K at pressures up to 800 MPa. *J. Phys. Chem. Ref. Data* 25 (6), 1509–1596.
- Terakawa, T., Miller, S.A., Deichmann, N., 2012. High fluid pressure and triggered earthquakes in the enhanced geothermal system in Basel, Switzerland. *J. Geophys. Res.: Solid Earth* 117 (B7).
- Tewksbury-Christle, C.M., Behr, W.M., 2021. Constraints from exhumed rocks on the seismic signature of the deep subduction interface. *Geophys. Res. Lett.* 48 (18).
- Tinti, E., Bizzarri, A., Piattesi, A., Cocco, M., 2004. Estimates of slip weakening distance for different dynamic rupture models. *Geophys. Res. Lett.* 31 (2).
- Tinti, E., Spudich, P., Cocco, M., 2005. Earthquake fracture energy inferred from kinematic rupture models on extended faults. *J. Geophys. Res.: Solid Earth* 110 (B12).
- Tse, S.T., Rice, J.R., 1986. Crustal earthquake instability in relation to the depth variation of frictional slip properties. *J. Geophys. Res.: Solid Earth* 91 (B9), 9452–9472.
- Vermeer, P., 1998. Non-Associated Plasticity for Soils, Concrete and Rock In Physics of Dry Granular Media. Springer, pp. 163–196.

- Viesca, R.C., 2021. Self-similar fault slip in response to fluid injection. *J. Fluid Mech.* 928, A29.
- Viesca, R.C., Dublanchet, P., 2018. The slow slip of viscous faults. *J. Geophys. Res.: Solid Earth* 124, 4959–4983.
- Viesca, R.C., Garagash, D.I., 2015. Ubiquitous weakening of faults due to thermal pressurization. *Nat. Geosci.* 8 (11), 875–879.
- Wang, L., Barbot, S., 2020. Excitation of san andreas tremors by thermal instabilities below the seismogenic zone. *Sci. Adv.* 6 (36), eabb2057.
- Yang, Y., Dunham, E.M., 2021. Effect of porosity and permeability evolution on injection-induced aseismic slip. *J. Geophys. Res.: Solid Earth* 126 (7) e2020JB021258.
- Yarushina, V.M., Podladchikov, Y.Y., 2015. (De)compaction of porous viscoelastoplastic media: model formulation. *J. Geophys. Res.: Solid Earth* 120 (6), 4146–4170.
- Yi, J.T., Li, Y.P., Bai, S., Fu, Y., Lee, F.H., Zhang, X.Y., 2018. A simple effective stress approach for modeling rate-dependent strength of soft clay. *J. Offshore Mech. Arctic Eng.* 140 (4).
- Zhu, W., Allison, K.L., Dunham, E.M., Yang, Y., 2020. Fault valving and pore pressure evolution in simulations of earthquake sequences and aseismic slip. *Nat. Commun.* 11 (1), 1–11.
- Zimmerman, R.W., Somerton, W.H., King, M.S., 1986. Compressibility of porous rocks. *J. Geophys. Res.: Solid Earth* 91 (B12), 12765–12777.
- Zoback, M.D., Gorelick, S.M., 2012. Earthquake triggering and large-scale geologic storage of carbon dioxide. *Proc. National Acad. Sci.* 109 (26), 10164–10168.